

P-T-t-d HISTORY OF THE GREATER HIMALAYA SEQUENCE IN THE
ZANSKAR SHEAR ZONE, NW INDIA

AS
36
2014
GEOL
-B43

A thesis submitted to the faculty of
San Francisco State University
In partial fulfillment of
The Requirements for
The Degree

Master of Science
In
Geosciences

By

Emma Nye Beck

San Francisco, California

May, 2014

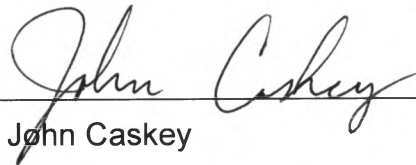
CERTIFICATION OF APPROVAL

I certify that I have read P-T-t-d History of the Great Himalaya Sequence in the Zaskar Shear Zone, NW India by Emma Nye Beck, and that in my opinion this work meets the criteria for approving a thesis submitted in partial fulfillment of the requirements for the degree: Master of Science in Geology at San Francisco State University.



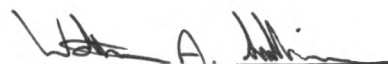
Dr. Mary Leech

Associate Professor of Geology



Dr. John Caskey

Associate Professor of Geology



Dr. Walter (Bill) Sullivan

Assistant Professor of Geology

Colby College

P-T-t-d HISTORY OF THE GREATER HIMALAYA SEQUENCE IN THE
ZANSKAR SHEAR ZONE, NW INDIA

Emma Nye Beck
San Francisco, CA
2014

Pressure-temperature-time-deformation (P-T-t-d) conditions describe the evolution of the Great Himalaya Sequence (GHS) deformed and exhumed along the Zaskar Shear Zone (ZSZ), the westernmost arm of the South Tibetan Detachment that spans the entire Himalayan range. Malung Tokpo samples are increasingly sheared nearing the ZSZ, developing an S-C foliation with shear banding. The dominant mineralogy is $Qz + Kfs + Pl + Bt + Grt + Ilm \pm Sil(Fi) \pm Ms \pm Ky \pm St$. Perple_X-generated pseudosections yield a 4-stage clockwise P-T trajectory: (1) nearly isothermal burial; (2) progressive temperature increase to peak P-T conditions, (3) near isothermal decompression, and (4) final exhumation. U-Pb SHRIMP dating of metamorphic and igneous zircon demonstrates that peak regional metamorphism conditions were reached at c. 25-20 Ma and that anatectic leucogranite crystallization continued to c. 23-18 Ma. Quartz CPOs suggest a progressive increase in deformation temperature with increased distance from the ZSZ, however absolute deformation temperatures are not designated due to the complex deformation history and degree of foliation development. The evolution of the GHS in Zaskar includes rapid burial (c. 33-27 Ma), closely followed by peak metamorphic conditions (c. 25-20 Ma), leading to a melt-weakened crust and relaxation-facilitated normal faulting through c. 21-18 Ma) and rapid exhumation. The P-T history of the GHS in Zaskar best matches channel flow model predictions but the modeled T-t histories for critical taper and channel flow require further thermochronological and local heat flow measurements for comparison to the results of this study.

I certify that the Abstract is a correct representation of the content of this thesis.


Chair, Thesis Committee

5/15/14
Date

ACKNOWLEDGEMENTS

I would like to thank my advisor Dr. Mary Leech and my fellow researchers at San Francisco State University, Ozüm Basta and Theodore Burlick. Their guidance, insight, and collaboration were integral to the success of this project. Stanford University's Matthew Coble provided invaluable support at every step of the U-Pb SHRIMP-RG process. The love and patience of my friends and family have kept me grounded and sane through these two years; I wholly appreciate it.

TABLE OF CONTENTS

List of Tables.....	vii
List of Figures.....	viii
List of Appendices.....	ix
1. Introduction.....	1
2. Previous work in the Greater Himalayan Sequence and the Zaskar Shear Zone.....	3
2.1. Study Area – Malung Tokpo.....	6
3. Methods.....	7
3.1 Perple_X Modeling and Mineral Chemistries.....	7
3.2. Sensitive High Resolution Ion Microprobe – Reverse Geometry (SHRIMP-RG) Mass Spectrometry.....	8
3.3. Electron Backscatter Diffraction (EBSD).....	12
4. Sample Descriptions.....	13
4.1. ZH-12 Quartzofeldspathic gneiss (N 33°32.56', E 76°39.364').....	14
4.2. ZH-14 Mylonitized mica schist (N 33°35.189', E 76°41.779').....	14
4.3. ZH-15 Mylonitized mica schist (N 33° 35.201', E 76° 41.766').....	15
4.4. ZH-16 Ultramylonite (N 33° 35.189', E 76° 41.779').....	16
4.5. ZH-22 Quartzofeldspathic Orthogneiss (N 33° 35.046', E 76° 41.7052').....	16
4.6. ZH-24 Quartzofeldspathic gneiss (N 33° 35.0157', E 76° 41.6617')..	16
5. Pseudosections and P-T Path Estimation.....	17
6. U-Pb Metamorphic and Crystallization Ages.....	19

7. Quartz CPOs.....	20
Interpreting Deformation Temperatures.....	21
8. P-T-t-d Evolution.....	22
9. Application to Models of the Himalayan Range.....	25
References Cited.....	29
Figure and Appendices Captions.....	38
Figures.....	44
Tables.....	55
Appendices.....	59

LIST OF TABLES

Table	Page
1. Table 1.....	55
2. Table 2.....	56
3. Table 3.....	57
4. Table 4.....	58

LIST OF FIGURES

Figure	Page
1. Figure 1.....	44
2. Figure 2.....	45
3. Figure 3.....	46
4. Figure 4.....	47
5. Figure 5.....	48
6. Figure 6.....	49
7. Figure 7.....	50
8. Figure 8.....	51
9. Figure 9.....	52
10. Figure 10.....	53
11. Figure 11.....	54

LIST OF APPENDICES

Appendix	Page
1. Appendix I.....	59
2. Appendix II.....	60

1. Introduction

The Himalayan range is the largest active continental collision zone in the world and subsequently the subject of much investigation and debate regarding physical models for ongoing orogenic processes (Beaumont, 2004; Wobus et al., 2003; Grujic et al., 2002; Godin et al., 2006; Horton and Leech, 2013). South of the Indus-Yarlung suture zone, the basic structure of the range includes three major lithotectonic units separated two bounding faults. The Greater Himalayan sequence (GHS) is a high-grade metamorphic unit bound by two lower grade units: the Lesser Himalayan sequence (LHS) to the south, below the Main Central Thrust (MCT); and the Tethyan Himalayan sequence (THS) to the north, above the South Tibetan Detachment (STD; Fig. 1). The MCT and STD are two sub-parallel, north-dipping, opposite-sense shear zones (Fig.1; Yin and Harrison, 2000). Range-wide Barrovian metamorphism began with the collision of the Indian subcontinent with Asia at ~57 Ma (Leech et al., 2005); the characterization of the subsequent evolution of the range has involved extensive research efforts, with some data gaps still existing in the western Himalaya (Searle, 1986; Herren, 1987; Searle and Rex, 1989; Dezes et al., 1999; Walker et al., 1999; Walker et al., 2001).

Many models have been developed to determine how the GHS was emplaced and exhumed (Le Fort, 1975; Beaumont et al., 2001; Searle and Rex, 1989; Kohn, 2008; Kohn, 2013). The channel flow model requires concurrent movement along the STD and the MCT, focused erosion at the range front, and gravitational forcing from the Tibetan plateau to drive lateral extrusion and exhumation of the mid-crustal GHS (Nelson et al., 1996; Beaumont et al., 2001; 2004; Grujic et al., 1996; 2002; Godin et al., 2006; Jamieson et al., 2004; 2006) Other models suggest that an orogenic wedge developed during the Indo-Asian collision and experienced protracted in-sequence thrusting with a décollement

that migrated downward along with changes in wedge geometry or thickness. These models are collectively known as the critical taper model (Henry et al., 1997; Grasemann et al., 1999; Bollinger et al., 2006; Kohn, 2008; Kohn, 2013).

Qualities of the GHS satisfy many of the requirements for both the channel flow and critical taper models, however, some discrepancies exist. For example, the approaches for dating the timing of slip on the STD and MCT across the orogen vary widely; some authors constrain either a minimum or a maximum age using, for example, field relationships or monazite crystallization ages (Godin et al., 2006, and references therein). Estimates for activity on the STD range from 23 to 13 Ma in the eastern Himalaya to 26 to 16 Ma in the western Himalaya (Godin et al., 2006 and references therein). The summary of data in Godin et al. (2006) are derived from studies using a variety of analytical methods and mineral(s) dated, and the geologic significance of those ages is not considered. The time constraints for activity on the STD and the MCT are broadly Miocene but so variable that it cannot be determined whether these faults are associated with the formation of a mid-crustal channel at depth or with late-stage exhumation of the GHS (Epard and Steck, 2004; Jessup et al., 2006; Searle et al., 2006). The predicted P-T and T-t evolution of the GHS and the LHS according to the channel flow and critical taper models also differ significantly, and as such require further research.

This study investigates the petrologic, structural, and geochemical characteristics of the GHS, to understand how these rocks and their histories in the Zaskar region of the western Himalaya correspond with central and eastern Himalaya. Correlation of the features of the GHS (i.e., age, phase equilibria, and structure) to other areas in the Himalaya requires a detailed reconstruction of its burial and exhumation history to understand the interplay of the shear zones with the major lithologic units. This study puts forth comprehensive characterization of

the pressure-temperature-time-deformation (P-T-t-d) history of the GHS, which combines petrologic characterization and thermodynamic modeling, geo/thermochronology, and microstructural analysis using electron backscatter diffraction. I find the P-T-t-d history of the Zaskar GHS requires elements of both the channel flow and critical taper models for the evolution of the Himalayas (Beaumont et al., 2001; Godin et al., 2006; Jessup et al., 2006; Searle et al., 2006; Kohn, 2008; Kohn, 2013; Finch et al., 2014).

2. Previous Work in the Greater Himalayan Sequence and the Zaskar Shear Zone

The GHS is a high-grade structural-metamorphic unit that is deformed in the footwall of the STD (Fig. 1). The STD is a range-wide, E-W trending, normal fault that forms a structural boundary between the THS to the north and the GHS to the south (Fig. 1). The Zaskar Shear Zone (ZSZ) is the western extension of the STD (Fig. 1). The upper portion of the GHS deformed in the ZSZ records an initial phase of top-to-the-south thrusting, prior to the formation of the top-to-the-north ZSZ (Grujic et al., 2002; Horton and Leech, 2013; Finch et al., 2014). Deformation in the ZSZ is broadly described as heterogeneous, non-coaxial (i.e. simple shear) plastic flow (Godin et al., 2006). The peak metamorphic assemblage within the GHS changes from NE to SW from Bt-Grt to Sil-Kfs (Herren, 1987; Kundig, 1989; Inger, 1998; Walker et al., 1999; 2001) The metamorphic isograds are condensed in a 200–250-m-thick mylonitized zone in central Zaskar. This telescoping began with the reactivation of the ZSZ in the mid-Miocene (Searle, 1986; Herren, 1987; Searle and Rex, 1989). Sm-Nd analyses of metamorphic garnets and U-Th-Pb analyses of metamorphic zircons indicate that peak regional metamorphism in the GHS likely occurred in Zaskar between 33–27 Ma (Table 1; Searle, 1986; Searle and Rex, 1989; Vance and Mahar, 1998; Horton and Leech, 2013). Metamorphic anatexis and leucogranite

generation in the GHS is constrained to ~24–19.5 Ma based on U-Pb analyses of zircon from deformed leucogranites and migmatites (Table 1; Noble and Searle, 1995; Walker et al., 2001; Horton and Leech, 2013; Finch et al., 2014).

Preliminary muscovite and biotite $^{40}\text{Ar}/^{39}\text{Ar}$ ages from Suru valley leucogranites of ~20–19 Ma and ~15 Ma, respectively, help constrain the timing of exhumation of the GHS. Apatite fission-track ages from the GHS suggests that the unit cooled above ~120°C between 8.1 ± 0.4 and 11.0 ± 0.3 Ma (Sorkhabi et al., 1997). These ages provide a lower age bound for deformation along the ZSZ.

Thermobarometric analyses of GHS rocks exposed along the STD are limited to conventional thermobarometry. Vance and Mahar (1998) generate isochemical phase diagrams, designated pseudosections for the remainder of the paper, using the program THERMOCALC. Their calculations yielded prograde garnet core-rim P-T conditions of ~500–700°C at 3–7 kbar. Estimated peak metamorphic conditions in Zaskar vary based on the technique. THERMOCALC-estimated peak conditions range from ~550–650°C and 5–7.5 kbar (Finch et al., 2014) to 620–650°C at 9.5–10.5 kbar (Walker et al., 2001). Dèzes et al. (1999) estimated higher peak temperatures of 750–850°C at 10–11 kbar using garnet exchange thermometers and barometers (GARC-GAPC).

Perple_X is a thermodynamic modeling program that calculates the stability fields for mineral assemblages in a specific rock sample based on its bulk composition over a set temperature and pressure range (Holland and Powell, 1998; Caddick and Thompson, 2008; Connolly, 2009). Leloup et al. (2010) modeled P-T paths using Perple_X and garnet geochemistries for GHS rocks in the STD of eastern Nepal. Peak conditions of 5–6 kbar and 550–650°C were calculated. Groppo et al. (2009) constructed pseudosections using Perple_X to determine P-T paths of GHS rocks deformed by the MCT in central Nepal and

found increasing P-T conditions further from the shear zone (545°C at 6.5 kbar to 790°C at 10 kbar).

Quartz CPO data and recrystallization mechanisms are used to estimate deformation conditions. Quartz CPOs are predominantly controlled by temperature, strain rate, and water content and are often used to infer deformation temperatures assuming a constant strain rate and fixed water content based on normal geologic conditions (Stipp et al., 2002a,b). The slip-systems associated with the quartz CPOs are activated preferentially depending on the temperature, strain rate and water content in the system. Temperature and strain rate have an inverse relationship, assuming constant water content (Stipp et al., 2002a,b). The slip-systems in order of decreasing temperature are: c-direction of slip, prism $\langle a \rangle$ slip, rhomb $\langle a \rangle$ slip, and basal $\langle a \rangle$ slip. Finch et al. (2014) identified quartz that dynamically recrystallized via grain boundary migration (GBM) and subgrain rotation (SGR) recrystallization. C-axis data from deformed leucogranites indicate a shift from lower greenschist-facies conditions (~500–600°C) to upper amphibolite-facies conditions (~650–700°C) according to their dominant slip systems (rhomb $\langle a \rangle$ and prism $\langle a \rangle$)(Finch et al., 2014). These data were acquired from quartz that was deformed within micaceous layers. Mineralogic heterogeneity, porphyroblast formation, and foliation development could control the CPOs of the deformed quartz grains. Consideration of these elements is important in assessing the validity of the assumed temperature values associated with the dominant slip systems (Law et al., 2011). This study attempts to determine the role that deformation history and foliation development play in the deformation and recrystallization of quartz to better understand its applicability to inferring deformation conditions (Stipp et al., 2002b; Law et al., 2011).

2.1. Study Area – Malung Tokpo

The GHS is well-exposed in Zaskar along a transect that follows the Suru River from the Suru dome in the northwest to the glacial valleys emptying into the Doda River in the southeast towards Padum (Fig. 2). This study focuses on samples collected along Malung Tokpo (~10 km southwest of Padum) where the ZSZ outcrops along a faceted range front parallel with the Doda River to the northeast. High-grade rocks of the GHS comprise the footwall of the ZSZ. The poorly-consolidated THS, known as the Phe Formation, forms the hanging wall to the north of the 2.3–6.8 km-thick ZSZ (Fig. 1, 2; Herren, 1987). The GHS in the Zaskar region is comprised of multi-stage Paleozoic granitic intrusions, anatectic migmatite and leucogranite, and gneiss, broadly known as the Kade Orthogneiss, and metapelites. The metapelites are the dominant lithology adjacent to the ZSZ and exhibit common 10–40-cm-thick quartz-rich intrusions in the way of veins and dikes. The degree of deformation recorded in the metapelites (determined using grain-size reduction, the intensity of shear bands, and the prevalence of boudinaged veins) increases toward the ZSZ. Foliation and lineation data is presented in Figures 1 and 2. Isoclinal and recumbent microfolding is abundant in the mylonites and quartz veins while large-scale folds are more prevalent in the structurally deeper part of the unit. As deformation becomes more intense from SW to NE, the metapelites progress from protomylonites to mylonites with S and C planes that become increasingly parallel. The microstructure and mylonitic foliations record top-to-the-NE, normal-sense motion but have been reported to also preserve an initial top-to-the-SW thrust sense movement (Horton and Leech, 2013; Finch et al., 2014). Deformed anatectic leucogranites are present throughout the unit but are more abundant within the ZSZ (Herren, 1987; Searle and Rex, 1989; Pognante et al., 1990; Dezes et al., 1999; Finch et al., 2014). The generation of these leucogranites has

been attributed both to shear heating (Harrison et al., 1998), and dehydration and decompression melting (Davidson et al., 1997; Finch et al., 2014).

3. Methods

This study uses three approaches to characterize the GHS in the footwall of the ZSZ. Data and observations presented here constrain the exhumation path, timing of metamorphism and exhumation, and deformation mechanisms recorded by recrystallized quartz grains in these high-grade rocks in the Himalayan core.

3.1 Perple_X Modeling and Mineral Chemistry

I developed four thermodynamic models for metamorphic rocks from the GHS to determine the P-T conditions experienced during burial and exhumation beneath the ZSZ. Samples were taken along a transect that extends from 10 m to the uppermost part of the ZSZ to 6 km southward into Malung Tokpo (Fig. 1; Table 2). Only samples containing aluminosilicates were selected for modeling because their role in the metamorphic reactions makes them essential for determining P-T paths.

Pseudosections were generated following the methodology of Connolly (1990) (Perple_X Version 07) in the MnNCKFMASHTO system using bulk-rock chemistries of samples ZH-12, ZH-14, ZH-15, and ZH-24 (Table 3). Solution phases were chosen for white mica (Mica(CHA); Auzanneau et al., 2009), chlorite (Chl(HP); Holland et al., 1998), staurolite (St(HP); Holland and Powell, 1998), cordierite (hCrd; Holland and Powell, 1998), garnet (Gt(WPH); White et al., 2000), and ternary feldspar (feldspar; Fuhrman and Lindsley, 1988). The reach_increment values for feldspar, Mica(CHA), and Gt(WPH) were increased to 6, 4, and 2, respectively, to eliminate spurious solvi. The phases oilm, and tbit were excluded to produce rutile and ilm_nol was excluded because it should only be present when using the Ilm(WPH) model (White et al., 2000).

Mineral chemistry data were collected from the same samples to look for zoning in garnet and to calculate temperatures using Fe-Mg exchange between garnet and biotite. Garnet and biotite chemistries were collected on a JEOL JXA-8230 electron microprobe in the Mineral Analysis Facility at Stanford University (Table 4). Garnet in samples ZH-14 and ZH-15 is generally homogeneous while garnets in ZH-24 are weakly zoned in the Sps (8–5) and Prp (9–7) and ZH-12 garnets exhibit zoning in the Alm (61–57) and Prp (31–23) components. To more accurately model ZH-12, the average garnet core chemistry was removed from the bulk-rock chemistry and the values were then normalized to 100% (Zuluaga et al., 2005). Isoleths for the Alm-, Prp-, Sps-, and Grs-components of garnet were calculated for the cores and rims of garnets in all samples and are shown plotted on the pseudosections in Appendix I. Complete transects across garnets are not possible due to the high incidence of inclusions and deformation (non-hexagonal cross-section). The result of a 5-point core-to-rim analysis of ZH-12 is presented in Figure 3. Biotite inclusions in garnet and matrix biotite chemistries were used to calculate core and rim temperatures with the corresponding garnets using the methods of Ferry and Spear (1978) and Hodges and Spear (1982).

3. 2. Sensitive High Resolution Ion Microprobe – Reverse Geometry (SHRIMP-RG) Mass Spectrometry

Zircon U-Pb depth-profiling analyses were conducted in the U.S. Geological Survey and Stanford University SHRIMP (SUMAC) facility at Stanford University. Six Metamorphic and igneous samples from throughout Zanskar (Malung Tokpo, Haptal Tokpo, and the Suru River valley) were analyzed in this investigation (Fig. 1; Table 1, 2).

Zircon age standard Temora-2 (416.8 Ma; Black et al., 2004) and an in-house compositional standard (MADDER) were co-mounted with unknown zircons. Standard grains were pressed into soft indium metal held in a 25-mm-

diameter, 4-mm-thick aluminum disk, which was then ground and polished to a 1-micron finish. Unknown zircon grains, concentrated by standard heavy mineral separation processes, were hand selected and mounted on glass slides coated in a thin (<10 microns) film of vacuum grease. This grease allows the grains to be easily manipulated and arranged in c. 1 x 6-mm rows with the flat euhedral zircon surfaces (m-face) oriented down, against the glass. Oriented zircon grains were pressed into the pre-polished indium, exposing flat non-polished zircon surfaces parallel with the mount surface and standard grains. Three mounts (ZH-1 and ZH-2) were created and zircon U-Pb ages were measured over three, two-day sessions.

All grains were imaged with reflected light on a petrographic microscope, and Temora-2 with cathodoluminescence (CL) on a JEOL 5600 SEM to identify internal structure, inclusions, and physical defects. The mounted grains were submerged in acetone to remove mounting grease, scrubbed with soap and water, and rinsed in dilute ethylenediaminetetraacetic (EDTA) acid and distilled water, dried in a vacuum oven, and coated with Au. The mounts were stored at high pressure (10^{-7} torr) for several hours before being moved into the source chamber of the SHRIMP-RG to minimize degassing of the epoxy and isobaric hydride interferences and masses 204-208.

Secondary ions are generated from the target spot with an O_2^- primary ion beam varying in intensity from 2.5 to 3.5 nA. The typically primary ion beam was defocused to achieve a spot diameter between 20-25 microns and a depth of ~2-4 microns. The Au was removed from the sample surface by pre-sputtering the primary beam for 30 seconds before data were collected. Measurements were made at mass resolutions of $M/\Delta M = 8000-8500$ (10% peak height), which eliminates interfering molecular species. The acquisition routine included high-mass normalizing species ($^{90}Zr_2^{16}O^+$), followed by $^{180}Hf^{16}O^+$, $^{204}Pb^+$, a

background measured at 0.046 AMU above the $^{204}\text{Pb}^+$ peak, $^{206}\text{Pb}^+$, $^{207}\text{Pb}^+$, $^{208}\text{Pb}^+$, $^{238}\text{U}^+$, $^{232}\text{Th}^{16}\text{O}^+$, and $^{238}\text{U}^{16}\text{O}^+$. All peaks were measured on a single EPT® discrete-dynode electron multiplier operated in pulse counting mode. Each mass was counted for 2, 1, 2, 10, 20, 10, 1, 5, 2, 4 seconds, respectively, with emphasis placed on measuring ^{206}Pb , ^{207}Pb , and ^{238}U . Because the U-Th concentration and age can change as the analysis depth profiles increase with time, we attempted to analyze ^{206}Pb and ^{238}U as close together in time as possible to avoid mixing different domains.

All analyses were performed with 5 scans by peak-hopping from mass 195.8 through 254. The primary focus was measuring ages from zircon rims, which can be less than 2 microns thick, based on the cross-sectional CL images of polished zircon crystals. Therefore, for individual analyses for which the age increased more than c. 20 Ma over the 5 cycles of data acquisition (i.e., depth profiling into an older age domain with depth), only the youngest 2, 3, or 4 cycles were used to calculate model ages (Fig. 4; Appendix II). To determine whether the old ages were in fact representative of the rim ages or whether they were a result of depth profiling through thin rims, zircon grains that indicated young ages were reanalyzed using a low beam current and large spot size, effectively decreasing the amount of the sample that was ablated thereby slowing the effects of depth profiling. A 45-scan test analysis indicated that depth-profiling occurred and that it is likely the largest source of error in the analyses. Common Pb contamination accounts for a smaller, secondary source of error.

U-Pb ages determined by SIMS are calculated relative to age standards, and are reliant upon the assumption that the standards are treated in the same manner as the unknowns. Therefore, the data was reduced using two methods: (1) the U-Pb calibration constant was calculated using 5 cycles of Temora-2 data for unknown analyses that yielded Tertiary ages from 4 or 5 cycles, or (2), for

analyses in which only 2 or 3 cycles of Tertiary ages were recorded, the U-Pb calibration constant was calculated using 3 cycles of Temora-2 data. The calibration constant for Temora-2 calculated using 3 versus 5 cycles differed by 0.06 to 1.28%. Given the 1-2% uncertainty in the ages of individual analyses, the calculated model ages are insensitive to the treatment of standard data, and much more sensitive to variations in the $^{206}\text{Pb}/^{238}\text{U}$ and U-concentrations with depth. Zircon concentration data for Hf, U, and Th are standardized against well-characterized, homogeneous in-house zircon standards MADDER (3435 ppm U, calculated relative to MAD-green (Barth and Wooden, 2010).

Calculated model ages for zircon are standardized relative to Temora-2, which were analyzed repeatedly throughout the duration of the analytical session (every 4th analysis). Data reduction for geochronology followed the methods described by Williams (1997) and Ireland and Williams (2003), and used the MS Excel add-in programs Squid2.51 and Isoplot3.76 of Ludwig (2009, 2003). The measured $^{206}\text{Pb}/^{238}\text{U}$ was corrected for common Pb using ^{207}Pb . The common-Pb correction was based on a model Pb composition from Stacey and Kramers (1975). All reported $^{206}\text{Pb}/^{238}\text{U}$ and $^{207}\text{Pb}/^{206}\text{Pb}$ model ages and uncertainties (2σ) include error summed in quadrature from the external reproducibility (1σ SD) of the standard Temora-2 during an individual analytical session (16-24 hours). To mitigate any skew caused by the depth profiling, grains were systematically excluded from these calculation if their 1σ errors were greater than 10% of the $^{206}\text{Pb}/^{238}\text{U}$ calculated ages as were analyses with errors $>15\%$ for the total $^{206}\text{Pb}/^{238}\text{U}$ count. Some grains that did not meet these criteria were still included when there were a small number of analyses to decrease the error in the calculated age, thereby strengthening the quality of the age calculation. The trend lines on Terra-Wasserberg diagrams are all anchored at a $^{207}\text{Pb}/^{206}\text{Pb}$ ratio of 0.837 based on the Stacey-Kramer model (Figs. 8, 9). This value is used for all

samples because of the limited number of grains in some samples, which, if data controlled, the trend line would not be representative of an actual $^{207}\text{Pb}/^{206}\text{Pb}$ ratio trend. This anchored projection line also provides a common reference frame for sample-to-sample comparisons. Grains that plot on this line, above the concordia line, have calculated ages that incorporate a common lead correction. Only the ages determined from the weighted averages calculations are reported in the text for consistency. A summary of the U-Pb results used in the age calculations is presented in Appendix II.

3.3. Electron Backscatter Diffraction (EBSD)

C-axis-fabric maps were generated using a Carl Zeiss Ultra 55 Field Emission Scanning Electron Microscope (FE-SEM) equipped with a HKL Nordlys II Electron Backscatter Diffraction (EBSD) detector at the Electron Microscopy Facility at San Francisco State University. Sample ZH-14 was mapped with the SEM at Bowdoin College equipped with a HKL Nordlys II detector and Channel 5 software (software details in Schmidt and Olesen, 1989). Samples were polished using a Vibromat vibratory polisher with 0.5-micron, non-crystallizing colloidal silica solution for c. 2–4 hours. They were then cleaned in an ultrasonic bath, dried, and sputter-coated with 10 nm of gold. Repolishing for five minutes ensured the surficial imperfections (e.g., grain boundaries, fractures, etc.) were filled with gold to create a more even surface for carbon coating. The samples were then coated with carbon to a thickness of ~4 nm to prevent sample charging.

Representative areas of thin sections were analyzed at a 70° stage tilt. Operating settings for the SEMs included an accelerating voltage of 20 kV, a beam current of 120 nA, and a working distance of 20 mm. Data acquisition and analysis with HKL Channel 5 software was used with 2x2 and 4x4 binning, high gain, 6 frames averaged, Hough resolution of 65 and 90 frames per second.

Settings varied based on mineralogy, sampling area, and microscope pre-set values. For sample indexing, the maximum MAD is 1.2, and a minimum of 5 and a maximum of 6 bands were used. The match units used were quartz, anorthite (for all feldspars to resolve indexing issues), muscovite, biotite, kyanite, sillimanite, and garnet. Indexing was 80% or better with the poor-indexing areas attributed to grain size, cracks or pitting in the sample due to mineral dissolution, and/or highly distorted crystal lattices in highly deformed areas.

The resulting crystallographic orientation maps were analyzed in the Channel 5 Program Tango and were characterized using different mapping functions such as band contrast, Euler angles ϕ_1 , Φ , ϕ_2 , and misorientation across grain boundaries of 5°, 10°, 20°, 40°, and 60° for each map. Data processing included extrapolating data points based on the orientation of 6 neighboring grains and reducing noise. Grains were detected with grain boundary completion down to 5° and minimum misorientation values of 10° though some other workers use misorientation angles up to 15° (White, 1977; Stipp and Kunze, 2008). Misorientation values of 60° in the {1010} plane within quartz grains were ignored as those can be attributed to Dauphiné twinning. The "large" and "small" grain subsets were chosen based on the approximated ellipse-fit grains. Grains that were less than 3x3 pixels, regardless of the designated step-size, were excluded unless verified as present using the band contrast map. Quartz $\langle c \rangle$ and $\langle a \rangle$ axis pole figures were plotted on lower-hemisphere, equal-area stereoplots using the Channel 5 Program Mambo.

4. Sample Descriptions

Eight samples from Malung Tokpo are included in this study. These were analyzed using multiple techniques (e.g., pseudosection modeling, EBSD, and/or U-Pb dating). Sampling was focused near the ZSZ to capture deformation in the mylonitized shear zone in the area of telescoped isograds (Fig. 5; Table 2). One

weakly deformed leucogranite (ZH-25) and one undeformed, cross-cutting leucogranite (ZH-9) from Malung Tokpo are also included in this study (Table 2). The leucogranites generally contain the same mineral assemblage PI + Kfs + Qz + Bt + Ms + Tur. Top-to-the-south shear sense indicators were not observed in the samples used in this study, unlike in Horton and Leech (2013) and Finch et al. (2014). Mineral abbreviations are after Whitney and Evans (2010) with the modification of fibrolite to Sil(Fi). Data for all samples are summarized in Table 2.

4.1. ZH-12 Quartzofeldspathic gneiss (N 33° 32.56', E 76° 39.364')

This sample is a quartzofeldspathic gneiss with the assemblage Qz + PI + Bt + Ky + Kfs + Grt + Rt + Sil(Fi) + Ilm + Ap. Biotite is dispersed among the large (0.5–3 mm diameter), dynamically-recrystallized quartz and feldspar grains. Quartz grains have well-defined sutured grain boundaries with minimal internal subgrain formation. Myrmekite intergrowths occur along the periphery of many plagioclase grains (Fig. 6b). Wide cordierite coronae surround kyanite within biotite, quartz, and plagioclase grains (Fig. 6a). Sillimanite forms a single mass of fibrolite identifiable in thin section. Inclusion-rich garnets are slightly retrograded to biotite and have maintained their zoning: compositions range from Alm₅₇Sps₈Grs₃Prp₃₁ in their cores to Alm₆₁Sps₁₅Grs₁Prp₂₀ in their rims.

4.2. ZH-14 Mylonitized mica schist (N 33° 35.189', E 76° 41.779')

The assemblage in this sample consists of Qz + PI + Kfs + Bt + Ms + Grt + Tur + Rt + Sil(Fi) + Ilm + St. Biotite and muscovite define type-I S-C foliation planes that reflect a top-to-the-NE deformation history with shear bands oriented ~45–55° to the C-planes (Fig. 5b, 6c; for S-C mylonite classification see Lister and Snoke, 1984). This shear banding also occurs in samples ZH-15, ZH-22, and ZH-24. Garnet occurs as a matrix mineral and as porphyroclasts while σ -type garnet porphyroclasts are aligned with the S-planes. Some garnets exhibit

extensional fractures sympathetic with top-to-the-NE extension (Fig. 6c). The garnets in both domains are unzoned, $\text{Alm}_{70}\text{Sps}_{12}\text{Grs}_8\text{Prp}_{19}$ in composition and contain abundant inclusions (Fig. 6c). Staurolite and garnet have similar growth relationships and probably record the prograde history of ZH-14. Minor fibrolite is aligned parallel with the foliation planes, and grew after biotite. Ilmenite grains are aligned with and cross-cut foliation planes suggesting growth pre- and post-deformation. Recrystallized quartz grains are ~ 0.25 mm in diameter in the S domains and ~ 0.1 mm in diameter in the C domains. Quartz grains exhibit sweeping undulose extinction with internal subgrain development in larger grains. Serrated quartz grain boundaries are characteristic of grain boundary bulging recrystallization.

4.3. ZH-15 Mylonitized mica schist (N 33° 35.201', E 76° 41.766')

ZH-15 lies structurally below ZH-14 but is approximately the same distance from the ZSZ and contains the same mineral assemblage. It has a well defined type-I S-C structure with biotite, muscovite, and minor fibrolite aligned within the S and C foliation planes and indicate top-to-the-NE shearing. Staurolite grains exhibit undulatory extinction and align with the S and C domains (Fig. 6e). Fibrolite lies parallel with the foliation planes and grew after staurolite, as demonstrated by the presence of fibrolite in the space between a pulled-apart staurolite grain (Fig. 6f). Garnet is abundant throughout the sample with several examples of garnet-biotite intergrowths and rotated garnet porphyroclasts. Garnet is weakly-zoned with compositions ranging from $\text{Alm}_{70}\text{Sps}_7\text{Grs}_{15}\text{Prp}_8$ in the cores to $\text{Alm}_{72}\text{Sps}_9\text{Grs}_{10}\text{Prp}_9$ in the rims. Recrystallized quartz grains range in size from ~ 0.5 – 0.1 mm in diameter (S-domain) to 0.1 – 0.01 mm (C-domains). The C-planes are separated by ~ 0.2 – 0.6 mm. Quartz grains are entirely recrystallized and exhibit subgrain development within the C domains and the serrated grain

boundaries around grains that exhibit sweeping undulose extinction in the S domains.

4.4. ZH-16 Ultramylonite (N 33° 35.189', E 76° 41.779')

ZH-16 is a type-II S-C mylonite collected from the highest structural level in the GHS, relative to other sample locations in this study. It contains the mineral assemblage Qz + Pl + Kfs + Bt + Ms (Fig. 5b). It is primarily composed of ≤ 0.1 mm-size recrystallized quartz and feldspar grains that likely experienced grain-size reduction via stress-induced solution transfer. Biotite and minor muscovite form the S-C foliation planes that indicate top-to-the-NE motion. The C-planes are separated by ~ 0.1 mm.

4.5. ZH-22 Quartzofeldspathic Orthogneiss (N 33° 35.046', E 76° 41.7052')

ZH-22 is a type-I S-C mylonite with widely-spaced (0.5–2.0 mm) C-domains that indicate a top-to-the-NE shear sense (Fig 5b). The dominant mineral assemblage is Qz + Pl + Kfs + Bt + Ms, and this sample was collected from the staurolite zone mapped by Herren (1987). Quartz is entirely recrystallized and elongated parallel to the direction top-to-NE shearing. There are distinctly different recrystallization mechanisms (SGR and GBM) occurring in areas of shear localization causing a range in recrystallized grain size of ≤ 0.1 –0.5 mm in the C domains and 0.5–1.0 mm. The foliation planes are defined by biotite and minor muscovite.

4.6. ZH-24 Quartzofeldspathic gneiss (N 33° 35.0157', E 76° 41.6617')

The mineral assemblage in ZH-24 includes Qz + Pl + Kfs + Ms + Bt + Grt + Sil(Fi) + Tur + Chl + Ilm + Rt. The quartz grains are all recrystallized and exhibit subgrain development and lobate grain boundaries suggest recrystallization via subgrain rotation and grain boundary migration (Fig. 6h). The presence of island

grains is also indicative of grain boundary migration recrystallization. Most garnet is partially retrograded to chlorite but preserves its ilmenite and quartz inclusions. Garnet exhibits an atoll texture with biotite and quartz growing in embayments. Several garnets are strung out and aligned with the foliation that formed during top-to-the-NE movement. Retrograde chlorite is present within foliation planes and within extensional cracks in garnet or replacing garnet rims (Inset in Fig. 6c). Fibrolite grew after biotite along foliation planes (Fig. 6g). Ilmenite lies within and cross-cuts the foliation suggesting growth pre- and post-deformation. Biotite, white mica, and fibrolite are aligned within the foliation and form small inclusions in matrix minerals.

5. Pseudosections and P-T Path Estimates

ZH-14 and ZH-15 both exhibit initial stable assemblages of Bt + St + Pl + Ms + Grt + Ilm + Qz with later Sil(Fi) (Fig. 6c,e,f). Isopleths of homogeneous garnet the Alm₆₉₋₇₀, Sps₁₁₋₁₃, Grs₈, and Prp₉₋₁₀ components in ZH-14 indicate stability at 6-7 kbar, 580-600°C and the Alm₆₉₋₇₂, Sps₆₋₉, Grs₁₀₋₁₅, and Prp₈ components in ZH-15 suggest stability at 6.5-8.3 kbar, 560-600°C (see Appendix I). The isopleths are average core and rim chemistries plotted incorporating any chemical variation from core to rim, even minor (1-2%) zoning. Fe-Mg exchange thermometry using garnet and biotite yields temperatures ranging from 550-600°C at 5.5-9.0 kbar in ZH-14 (Fig. 7a; Table 4) to 630-695°C for 5.5-9.0 kbar in ZH-15 (Fig. 7b; Table 4). The garnet and biotite chemistries are calculated using the average compositions for the garnets in ZH-14, ZH-15 and ZH-24 representing the prograde to peak temperature conditions. ZH-12 garnet-biotite thermometry was calculated twice using average core and average rim chemistries, representing peak to retrograde conditions. The growth relationships of garnet and staurolite indicate that in both ZH-14 and ZH-15 these minerals grew early in the P-T histories of these rocks. This suggests a nearly isothermal

increase in pressure followed by an increase in temperature. These samples record their highest temperatures with the growth of K-feldspar, which is associated with peak metamorphism at c. 800°C in ZH-14 and 850°C in ZH-15. A subsequent decrease in pressure and temperature allowed the retrograde fibrolite growth after staurolite and biotite in the foliation planes (Fig. 6f). Retrograde chlorite grew in the shear bands that indicate top-to-the-NE motion.

ZH-24 lies farther from the shear zone than ZH-14 and 15 (Fig. 7c). The weakly zoned garnet Alm_{80-81} , Sps_{5-8} , Grs_{3-4} , and Prp_{7-9} isopleths indicate initial stability at ~540-610°C and ~7.3-10.0 kbar. Minor core-rim zoning in the Prp and Sps components indicate an increase in temperature with growth (Appendix I). Fe-Mg exchange thermometry using garnet and biotite from ZH-24 generated higher temperatures of $700 \pm 50^\circ\text{C}$ at 5.5-9.5 kbar. Garnet and biotite growth was followed by formation of fibrolite, which suggests that temperature increased from the garnet isopleth stability range to the appearance of K-feldspar, then sillimanite, at peak metamorphic conditions of 8.5-9.5 kbar, ~800°C (Fig. 6g; 7). The presence of late-stage Ilm suggests that peak conditions were followed by a decrease in pressure, and retrograde chlorite within foliation planes and in extensional cracks in garnet grew at subsequently lower temperatures (Fig. 6c inset).

The prograde assemblage in ZH-12 includes Bt + Chl + Pl + Ms + Gt + Rt, followed by Ky growth at increased P-T conditions (Fig. 7d). K-feldspar and sillimanite grew at peak P-T conditions that correspond to calculated Grt-Bt temperatures of 850°C at 10 kbar for garnet cores and biotite inclusions. These are limited by the absence of muscovite in ZH-12 (Fig. 7d). Retrograde cordierite coronae around Ky grains grew as pressure decreased during exhumation. The zoned garnet $\text{Alm}_{57(\text{core})-61(\text{rim})}$, $\text{Sps}_{8(\text{core})-15(\text{rim})}$, $\text{Grs}_{1(\text{rim})-3(\text{core})}$, and $\text{Prp}_{20(\text{rim})-31(\text{core})}$ isopleths indicate a broad area of stability from 550-650°C at 6-9 kbar (Appendix

l). Fe-Mg exchange thermometry using garnet (core and rim) and biotite (inclusions and matrix) indicates a decrease in temperature from 850-870°C in the cores to 650-670°C in the rims.

6. U-Pb Metamorphic and Crystallization Ages

U-Pb SHRIMP analyses of zircon from an undeformed leucogranite dike (ZH-9; Malung Tokpo) yielded the largest number of Miocene ages and represent the most robust thermochronological dataset (Fig. 2; Fig. 5d; Fig. 8a,b; Table 1). These data yield an average age for ZH-9 of 21.5 ± 0.3 Ma. The individual analyses that meet the criteria outlined in Section 3.2 range from 23.8 ± 2 Ma to 18.1 ± 2 Ma. Deformed leucogranites in Haptal Tokpo and Malung Tokpo (Z-4 and ZH-25) yielded only four viable analyses with ages ranging from 25.2 ± 1.1 Ma to 20.8 ± 1.4 Ma (Fig. 1; Fig. 8c-f; Table 1). Zircon from metamorphic samples from Suru Valley, Nun Kun Valley, and the Suru dome yield ages of c. 22.2 ± 2.9 - 17.5 ± 5.3 Ma (Table 1). A mica schist from Suru valley (ZH-36) yielded 11 grains that generate ages of c. 21.6 ± 2.7 Ma (Fig. 1; Fig. 9a,b; Table 1). A schist from the Suru dome (ZH-41) yield slightly younger ages at c. 19.9 ± 0.9 Ma (Fig. 1; Fig. 9c,d). Three grains from a schist from the Nun Kun valley (Z-32) generated the youngest average ages of c. 17.2 ± 5.3 Ma (Fig. 1; Fig. 9e,f; Table 1). Horton and Leech (2013) reported U-Pb analyses of monazite and zircon for samples Z-4 and Z-32 that produce ages of 461 ± 21 Ma and 1100-995 Ma, respectively, reflecting inheritance in those samples; zircons from those same samples were reanalyzed in this study using the rim-sampling technique to obtain the most recent crystallization ages of overgrowths.

Due to the significant influence of depth profiling on the calculated U-Pb ages, it is difficult to generate a statistically strong dataset for the young metamorphic and crystallization events. Though this dataset is statistically weak,

it still bears geologic significance because the increase in ages with progressive scans is almost certainly a result of depth-profiling through the younger rims to an older zircon growth domain (Fig. 4). As such, the calculated Oligocene-Miocene crystallization and metamorphic ages are representative of the history of these samples and any older ages are inherited.

7. Quartz CPOs

Crystallographic preferred orientations (CPOs) of recrystallized quartz in samples collected in Malung Tokpo record a general change in dominant slip-systems associated with an increase in temperature. The CPOs recorded in these samples are not as strong as typical mylonites (Lister and Snoke, 1984). Weak CPOs are likely attributable to mica-dominated foliation controlling the deformation in the sample and the influence of multiple deformation mechanisms. Quartz in ZH-16 records a CPO weakly indicative of rhomb $\langle a \rangle$ slip (Fig. 10c; Table 1); activation on this slip system is associated with moderate temperatures (Schmid and Casey, 1986). This may not necessarily indicate specific deformation temperatures because the sample is intensely deformed and exhibits evidence for stress-induced solution transfer, which is characterized by weak CPOs (Bons and den Brok, 2000). Quartz in ZH-14 does not have a strong CPO when all data points are plotted (Fig. 10b). When plotted separately the larger quartz grains in ZH-14 have a stronger prism $\langle a \rangle$ slip signature and the smaller grains have a stronger c-slip signature, which are both associated with higher temperatures (Fig. 10h; Table 1; Mainprice et al., 1986; Schmid and Casey, 1986). The smaller quartz grains are generally located within the micaceous foliation planes and the larger grains are located between the mica-rich layers. Rotating the pattern orientation of the small grains 70° about the z-axis nearly replicates the orientation of the larger grains (Fig. 10h), suggesting that deformation of the smaller grains outlasted the larger grains in the

micaceous domains once a through going network of mica developed (Schmid and Casey, 1986). Quartz in ZH-15 predominantly records prism $\langle a \rangle$ slip with a slightly off-centered c-axis maximum (Fig. 10a), and there is little change in the quartz CPO between the small and large grain domains. The off-centeredness is likely due to the thin sections not being cut exactly perpendicular to foliation and/or parallel with lineation. Recrystallized quartz in ZH-22 records prism $\langle a \rangle$ slip in the small grains and both prism $\langle a \rangle$ and rhomb $\langle a \rangle$ slip in the large grains (Fig. 10g,i; Table 1). Quartz in ZH-24 records c-slip in both the large and small grain-size domains, and it is the structurally deepest sample in the transect that records a quartz CPO (Fig. 10f; Table 1). That depth corresponds to the higher temperatures associated with C-slip ($>650^\circ\text{C}$; Mainprice et al., 1986). Quartz in ZH-12 does not show a CPO (Fig. 10d; Table 1) and this is consistent with the relatively strain-free appearance of quartz grains in thin section (Fig. 6a,b).

Interpreting Deformation Temperatures

Quartz CPOs and their dominant slip systems are often used as indicators of deformation temperatures in ductilely-deformed rocks (e.g., Tullis and Yund, 1977; Bouchez et al., 1983; Mainprice et al., 1986; Schmid and Casey, 1986). Most microstructure-based thermometers assume average and constant geologic strain rates, which poses a problem in understanding shear zone development. Domainal variation in quartz recrystallization mechanisms, grain size, and mica content occurs in several samples. The operation of different recrystallization mechanisms is associated with different CPOs and requires plotting the S-domains (large grains) and C-domains (small grains) separately (Fig 10; Tullis and Yund, 1977; Mainprice et al., 1986; Schmid and Casey, 1986). Stipp et al. (2002a) uses the relationship between strain rate, deformation temperature, and dynamic recrystallization mechanisms to demonstrate that temperature and strain rate have an inverse relationship, and as such the “high T” CPOs operating

in the S domains more likely represent a decreased strain rate than higher deformation temperatures (Stipp et al., 2002a). The rotated CPOs, particularly in ZH-14 (Fig 11h), suggest that prolonged deformation occurred in the S domains as the foliation developed. As shearing on the ZSZ came to an end, quartz likely recrystallized at lower strain rates and on “high-temperature” slip systems (e.g., c-slip) in the S domains (ZH-22; Fig 10i). Three factors likely contributed to CPO variability: foliation development, mineralogic heterogeneity, and change in strain rate; without being able to exclude these factors from the system it is difficult to assign deformation temperatures based on quartz CPOs.

The GHS experienced multiple phases of deformation and leucogranite generation in close succession, which could affect recrystallization mechanisms and subsequently the inferred deformation temperatures, particularly in the samples deformed in the uppermost GHS (Law et al., 2011; Finch et al., 2014). Multiple phases of deformation are recorded at the macro- and microstructural scales (e.g., S-C foliation, shear banding, etc.) and as such it is difficult to ascribe a constant or average value of strain rate when assessing deformation temperatures. Progressive development of S and C foliation planes may change strain accommodation within the samples over time. I instead suggest relative temperature estimates rather than assigning absolute temperatures to deformation. Generally the quartz CPOs from the GHS preserve an increase in deformation temperatures moving south, which agrees with the observed mineral assemblages increasing in grade at lower structural levels.

8. P-T-t-d Evolution

My data and observations indicate that the P-T-t-d history of GHS samples collected in Malung Tokpo can be divided into four stages (Fig. 11):

Stage 1. Prograde staurolite in ZH-14 and ZH-15 indicates early, prograde P-T conditions of 4-6 kbar and 550-650°C (Stage 1 in Fig. 11; see also Figs. 6e, f; Z). ZH-14 and ZH-15 underwent near isothermal burial as they passed through garnet stability fields at ~6-7 kbar in ZH-14 and 7-9 kbar in ZH-15 (white ellipses in Fig. 7; Appendix I). Garnet in sample ZH-14 shows little to no elemental zoning and temperatures calculated using Fe-Mg exchange between garnet and biotite coincide with garnet isopleth modeling (Fig. 7; Table 4; Appendix I). Horton and Leech (2013) also report S-C fabrics and snowball garnets in micas schists from the Suru valley that show top-to-the-SW shear sense, preserving the early thrust history of rocks cut by the ZSZ. This prograde history likely occurred between ~33 and 27 Ma based on U-Pb ages of monazite and Sm-Nd ages of garnet (Stage 1 in Fig. 11; Vance and Harris, 1999; Horton and Leech, 2013). Thrusting in this area must have rapidly buried the GHS ~12 km to create the nearly isothermal conditions that are preserved in the prograde assemblages.

Stage 2. K-feldspar in ZH-14, ZH-15, and ZH-24, and kyanite in ZH-12 grew as P-T conditions increased toward a peak of ~800–850°C and 9–10 kbar (Stage 2 in Fig. 11; see also Figs. 6b and 7). This increase in temperature can be attributed to the crust equilibrating to ambient temperatures after burial, triggering anatexis melting in the mid-crust via metamorphic dehydration reactions. This magmatism was the catalyst for the onset of exhumation (Stage 3). These peak temperature conditions were reached at $\sim 21.6 \pm 2.7$ to 19.9 ± 0.9 Ma based on U-Pb depth-profile analyses of zircon from mica schists from Suru valley (Stage 2 in Fig. 11; Fig. 9). Finch et al. (2014) presents U-Pb ages from a deformed leucogranite (Stages 1–2) suggesting crystallization occurred around 24.0 ± 0.3 Ma while thrusting on rocks cut by the ZSZ was ongoing.

Stage 3. Late-stage sillimanite (fibrolite) grew in the necks of microboudinaged staurolite in ZH-15; fibrolite replaced biotite in ZH-14, ZH-24,

and ZH-12; and garnet shows extensional microfractures in ZH-14. This marks the onset of extension on the ZSZ (Stage 3 in Fig. 11; see also Figs. 6d,f,h and 7). Retrogression is also recorded in the relatively high-Mg, low-Fe cores of garnet in ZH-12 (Caddick et al., 2010). Continued leucogranite generation resulted in an increased melt fraction in the unit, which resulted weakening and transition to normal movement on the ZSZ (Kohn, 2008; Finch et al., 2014). Extensional movement is achieved in a thrust system when the rheology is changed. In this case, dehydration melting associated with thrusting could have weakened the crust, which lowered the critical taper angle and led to extensional faulting (Willett, 1999; Kohn, 2008; Finch et al., 2014). The initiation of tectonic exhumation likely increased leucogranite production via decompression melting. The first fabrics recording top-to-the-NE motion developed during this stage and these fabrics continued to develop through to Stage 4 (see Figs. 5; 6). Foliation intensity and quartz dynamic recrystallization decreases with distance from the shear zone (Fig. 5, 10).

U-Pb zircon ages acquired from leucogranites deformed during normal-sense, top-to-the-NE motion indicate that leucogranite crystallization occurred from 25.2 ± 1.1 Ma to 20.8 ± 0.9 Ma (Fig. 8, 11). A migmatite from the GHS yielded a U-Pb monazite age of 21.5 ± 1.0 Ma (Horton and Leech, 2013). These data indicate a 5–7 Ma window of time for the switch from a thrusting to an extensional system with abundant syn-tectonic leucogranite production. An undeformed, cross-cutting leucogranite (ZH-9) yielded U-Pb zircon ages ranging from 23.8 ± 1.8 to 18.1 ± 2.5 Ma, thus ductile deformation accommodating normal-sense motion must have ceased by this time. These results correlate well with the 23–21.5-Ma U-Pb ages from an undeformed leucogranite reported by Finch et al. (2014), and my data indicate that shearing on the ZSZ continued until as late as 18.1 ± 2.5 Ma (Figs. 5d; 8a; Table 1). Because my U-Pb ages were

collected by depth-profiling and because I have used only the youngest 2, 3, or 4 scan cycles to calculate model ages, my 18.1 ± 2.5 -Ma age is the most accurate constraint on the end of shearing on the ZSZ (Fig. 4; Appendix II).

Stage 4. Cordierite coronae around kyanite grains and myrmekite development in ZH-12 record decompression during exhumation (Stages 3-4 in Fig. 11; Fig. 6a,b). Fe-Mg exchange thermometry for garnet and biotite in ZH-12 gives temperatures of $\sim 860^\circ\text{C}$ for garnet cores and biotite inclusions, decreasing to $\sim 660^\circ\text{C}$ for garnet rims and matrix biotite, and this probably reflects the temperature decrease during exhumation (Stages 3–4 in Fig. 11; Fig. 7; Table 4). Retrograde chlorite within foliation planes and replacing garnet and biotite in ZH-14, ZH-15, and ZH-24 grew as a result of decreased temperatures (Stage 4 in Fig. 11; Figs. 6d; 7). Chlorite growth on garnet fractures indicates that normal movement on the ZSZ continued after the GHS cooled through brittle-ductile transition (Fig. 6d). Preliminary $^{40}\text{Ar}/^{39}\text{Ar}$ cooling ages from muscovite and biotite suggest rapid cooling through $\sim 400^\circ\text{C}$ at c. 20-19 Ma and through $\sim 300^\circ\text{C}$ at c. 15 Ma (Stage 4 in Fig. 11). Apatite fission-track ages demonstrate that GHS exhumed through the uppermost crust ($\sim 120^\circ\text{C}/3.25$ km) at of ~ 11 –8 Ma (Stage 4 in Fig. 11; Sorkhabi et al., 1997).

9. Application to Tectonic Models for the Himalaya

The four-stage history documented in this study indicates (1) thrusting on the ZSZ resulted in nearly isothermal burial of the Zaskar GHS; (2) heating to peak P-T conditions caused metamorphic dehydration reactions that caused in-situ leucogranite melting; (3) magmatism was a catalyst for exhumation that was likely further driven by accompanying decompression melting, and corresponded to the start of normal-sense motion on the ZSZ; and (4) rapid exhumation of the GHS through the middle crust was driven by simultaneous motion on the MCT and ZSZ through the Early Miocene, along with significant strength reduction in

the partially-molten GHS and monsoon-enhanced erosion in the foreland (Stages 1–4 in Fig. 11; Beaumont et al., 2004; Jamieson et al., 2004; Rosenberg and Handy, 2005; Godin et al., 2006)

The models for the evolution of the GHS are a topic of significant debate (Beaumont et al., 2004; Grujic, 2006; Kohn, 2008; Sachan et al., 2010; Carosi et al., 2013; Finch et al., 2014) with the channel flow and critical taper models being two prominent end-member models in the discourse. The geological and geophysical characteristics of the range can be reconciled with the majority of the properties of both models, however they differ in their predicted amount of displacement of the GHS, timing of the onset of exhumation, and the duration and rate of exhumation. Thermomechanical models for channel flow in the eastern Himalaya predict that the GHS took 20–30 Ma to reach peak temperatures and began retrogression and exhumation around 10 Ma (Godin et al., 2006; Jamieson et al., 2006). The models also require that during extrusion and exhumation, the GHS would have been displaced 100s of km along the MCT and STD (Godin et al., 2006a; Jamieson et al., 2006). Numerical models for critical taper shows that prograde, peak, retrograde metamorphism spanned a 10–15 Ma window of time (Kohn, 2008); and exhumation is predicted to have begun at ~20 Ma and displaced the GHS only 10s of km (see Fig. 11). Studies in the eastern (Bhutan) and central (Nepal) Himalaya estimate the horizontal displacement along the STD ranges from 30–40 km (Burchfield et al., 1992; Hodges et al., 1998) up to 90–108 km, calculated assuming a constant 10° dip of the STD and a 3.5 km/kbar pressure gradient (Grujic et al., 2002; Searle et al., 2003). In the Zaskar region, slip estimates for the ZSZ are ~25–35 km based on the geometry of the shear zone and the extent of isograd telescoping (Herren, 1987; Dezes et al., 1999; Searle et al., 1999; Walker et al., 1999; Finch et al., 2014). Displacement calculations on the STD vary range wide, completely satisfying neither model.

The P-T-t-d history generated in this study contains components that satisfy both the channel flow and critical taper model predictions. The P-T path trajectory of prograde to peak metamorphic conditions for this study broadly resembles the predicted conditions for both the channel flow and critical taper models, while the retrograde and exhumation history calculated in this study does not clearly align with either model (Fig. 11b,c). The geo/thermochronological analyses in this study indicate a two-stage exhumation using a model geothermal gradient of 37°C/km from Nábělek and Nábělek (2014). The first, faster exhumation stage calculated using U-Pb analyses for peak conditions (800°C at 10 kbar at ~25-20 Ma) through $^{40}\text{Ar}/^{39}\text{Ar}$ muscovite ages from the middle crust (400°C at 3.5 kbar at ~20-19 Ma) occurred at a faster rate (~15-20°C/km) than the final stages of exhumation from the middle to upper crust (~110°C at 1.1 kbar using AFT ages of ~11-8 Ma; ~1.0–1.5°C/km)(Fig. 11c). The STD was still active until at least 15 Ma in Zanskar based on preliminary $^{40}\text{Ar}/^{39}\text{Ar}$ dating of biotite for the Suru valley presented in this study and is supported by Godin et al. (2006) who use a compilation of all thermochronology for the western sections of the STD to show it stopped moving at c. 14–12 Ma. This supports a two-stage exhumation history for GHS rock but it is not indicated by the T-t trajectories predicted in the channel flow and critical-taper models (Fig. 11). The T-t plot in Figure 11 includes the thermal conditions during the development of the GHS according to the predictions of the thermomechanical models (channel flow: Jamieson et al., 2004; critical taper: Henry et al., 1997; Bollinger et al., 2006). The thermomechanical model presented by Jamieson et al. (2004) indicates that the onset of exhumation of the GHS occurred at ~10 Ma whereas the critical taper models, as described by Kohn (2008) initiate exhumation at ~15 Ma. These discrepancies between the models' predictions and the exhumation history developed in this study, make it difficult to assign one

best-fit model to Zanskar (Godin et al., 2006; Kohn, 2008; Sachan et al., 2010; Chambers et al., 2011; Finch et al., 2014). The trajectory of P-T paths generated in this study largely resembles those predicted by the channel flow model, particularly the early isothermal exhumation and contrasts with the hair-pin style P-T paths predicted by the critical taper model. If the channel flow model applied, the T-t path from this study suggests that the channel developed and reached peak temperatures more quickly than is predicted by the model (Jamieson et al., 2004; Godin et al., 2006). Further thermochronological studies will greatly enhance these comparisons and supplementing these data with more local heat flow measurements will enable better estimate model the modern geothermal gradient in the Zanskar region to calculate exhumation rates. Including these findings in the channel flow and critical taper thermomechanical models would better constrain the evolution of the GHS and increase the resolution with which we can reconstruct the history of the GHS.

References Cited

- Auzanneau, E., Schmidt, M.W., Vielzeuf, D., and D Connolly, J.A., 2009, Titanium in phengite: a geobarometer for high temperature eclogites: *Contributions to Mineralogy and Petrology*, v. 159, p. 1–24, doi: 10.1007/s00410-009-0412-7.
- Barth, A.P., and Wooden, J.L., 2010, Coupled elemental and isotopic analyses of polygenetic zircons from granitic rocks by ion microprobe, with implications for melt evolution and the source of granitic magmas: *Chemical Geology*, v. 277, p. 149–159.
- Beaumont, C., Jamieson, R.A., Nguyen, M.H., and Medvedev, S., 2004, Crustal channel flows: 1. Numerical models with applications to the tectonics of the Himalayan-Tibetan orogen: *Journal of Geophysical Research*, v. 109, doi: 10.1029/2003JB002809.
- Beaumont, C., Jamieson, R.A., Nguyen, M.H., and Lee, B., 2001, Himalayan tectonics explained by extrusion of a low-viscosity crustal channel coupled to focused surface denudation: *Nature*, v. 414.
- Black, L.P., Kamo, S.L., Allen, C.M., Davis, D.W., Aleinikoff, J.N., Valley, J.W., Mundil, R., Campbell, I.H., Korsch, R.J., Williams, I.S., and Foudoulis, C., 2004, Improved $^{206}\text{Pb}/^{238}\text{U}$ microprobe geochronology by the monitoring of a trace-element-related matrix effect; SHRIMP, ID-TIMS, ELA-ICP-MS and oxygen isotope documentation for a series of zircon standards: *Chemical Geology*, v. 205, p. 115–140, doi: <http://dx.doi.org/10.1016/j.chemgeo.2004.01.003>.
- Bollinger, L., Henry, P., and Avouac, J., 2006, Mountain building in the Nepal Himalaya: Thermal and kinematic model: *Earth and Planetary Science Letters*, v. 244, p. 58–71, doi: 10.1016/j.epsl.2006.01.045.
- Bons, P.D., and den Brok, B., 2000, Crystallographic preferred orientation development by dissolution–precipitation creep: *Journal of Structural Geology*, v. 22, p. 1713–1722.
- Bouchez, J.L., Lister, G.S., and Nicolas, A., 1983, Fabric asymmetry and shear sense in movement zones: *Geologische Rundschau*, v. 72, p. 401–419.
- Burchfield, B.C., Chen, Z., Hodges, K.V., Liu, Y., Royden, L.H., Deng, C., and Xu, J., 1992, The South Tibetan Detachment System, Himalayan Orogen:

Extension Contemporaneous with and Parallel to Shortening in a Collisional Mountain Belt: Geological Society of America Special Paper, v. 269, doi: 10.1130/SPE269-p1.

- Caddick, M.J., Konopasek, J., and Thompson, A.B., 2010, Preservation of Garnet Growth Zoning and the Duration of Prograde Metamorphism: *Journal of Petrology*, v. 51, p. 2327–2347, doi: 10.1093/petrology/egq059.
- Caddick, M.J., and Thompson, A.B., 2008, Quantifying the tectono-metamorphic evolution of pelitic rocks from a wide range of tectonic settings: Mineral compositions in equilibrium: *Contributions to Mineralogy and Petrology*, v. 156, p. 177–195.
- Carosi, R., Montomoli, C., Rubatto, D., and Visona, D., 2013, Leucogranite intruding the South Tibetan Detachment in western Nepal: implications for exhumation models in the Himalayas: *Terra Nova*, v. 25, p. 478–489.
- Chambers, J., Parrish, R., Argles, T., Harris, N., and Horstwood, M., 2011, A short-duration pulse of ductile normal shear on the outer South Tibetan detachment in Bhutan: Alternating channel flow and critical taper mechanics of the eastern Himalaya: Outer South Tibetan Detachment, Bhutan: *Tectonics*, v. 30, p. 1–12, doi: 10.1029/2010TC002784.
- Connolly, J.A.D., 2009, The geodynamic equation of state: what and how: *Geochemistry, Geophysics, Geosystems*, v. 10, doi: DOI:10.1029/2009GC002540.
- Davidson, C., Grujic, D.E., Hollister, L.S., and Schmid, S.M., 1997, Metamorphic reactions related to decompression and synkinematic intrusion of leucogranite, High Himalayan Crystallines, Bhutan: *Journal of Metamorphic Geology*, v. 15, p. 593–612.
- Dezes, P.J., Vannay, J.-C., Steck, A., Bussy, F., and Cosca, M., 1999, Synorogenic extension: Quantitative constraints on the age and displacement of the Zaskar shear zone (northwest Himalaya): *Geological Society of America Bulletin*, v. 111, p. 364–374.
- Epard, J.-L., and Steck, A., 2004, The eastern prolongation of the Zaskar shear zone (western Himalaya): *Eclogae Geologicae Helvetiae*, v. 97, p. 193–212.

- Ferry, J.M., and Spear, F.S., 1978, Experimental Calibration of the Partitioning of Fe and Mg Between Biotite and Garnet: *Contributions to Mineralogy and Petrology*, v. 66, p. 113–117.
- Finch, M., Hasalova, P., Weinberg, R.F., and Fanning, C.M., 2014, Switch from thrusting to normal shearing in the Zaskar shear zone, NW Himalaya: Implications for channel flow: *Geological Society of America Bulletin*, doi: 10.1130/B30817.1.
- Le Fort, P., 1975, Himalayas: The Collided Range. Present Knowledge of the Continental Arc: *American Journal of Science*, v. 275-A, p. 1–44.
- Fuhrman, M.L., and Lindsley, D.H., 1988, Ternary-feldspar modeling and thermometry: *American Mineralogist*, v. 73, p. 201–215.
- Godin, L., Grujic, D., Law, R.D., and Searle, M.P., 2006a, Channel flow, ductile extrusion and exhumation in continental collision zones: an introduction: Geological Society, London, Special Publications, v. 268, p. 1–23.
- Godin, L., Grujic, D., Law, R.D., and Searle, M.P., 2006b, Channel flow, ductile extrusion and exhumation in continental collision zones: an introduction: Geological Society, London, Special Publications, v. 268, no. 1, p. 1–23.
- Grasemann, B., Fritz, H., and Vannay, J.-C., 1999, Quantitative kinematic flow analysis from the Main Central Thrust Zone (NW-Himalaya, India): implications for a decelerating strain path and the extrusion of orogenic wedges: *Journal of Structural Geology*, v. 21, p. 837–853.
- Groppo, C., Rolfo, F., and Lombardo, B., 2009, P–T evolution across the Main Central Thrust Zone (Eastern Nepal): hidden discontinuities revealed by petrology: *Journal of Petrology*, v. 50, p. 1149–1180.
- Grujic, D., 2006, Channel flow and continental collision tectonics: an overview: Geological Society, London, Special Publications, v. 268, p. 25–37.
- Grujic, D., Casey, M., Davidson, C., Hollister, L.S., Kündig, R., Pavlis, T., and Schmid, S., 1996, Ductile extrusion of the Higher Himalayan Crystalline in Bhutan: evidence from quartz microfabrics: *Tectonophysics*, v. 260, p. 21–43.
- Grujic, D., Hollister, L.S., and Parrish, R.R., 2002a, Himalayan metamorphic sequence as an orogenic channel: insight from Bhutan: *Earth and Planetary Science Letters*, v. 198, p. 177–191.

- Grujic, D., Hollister, L.S., and Parrish, R.R., 2002b, Himalayan metamorphic sequence as an orogenic channel: insight from Bhutan: *Earth and Planetary Science Letters*, v. 198, p. 177–191.
- Harrison, T.M., Grove, M., Lovera, O.M., and Catlos, E.J., 1998, A model for the origin of Himalayan anatexis and inverted metamorphism: *Journal of Geophysical Research*, v. 103, p. 27,017–27,032.
- Henry, P., Le Pichon, X., and Goffé, B., 1997, Kinematic, thermal and petrological model of the Himalayas: constraints related to metamorphism within the underthrust Indian crust and topographic elevation: *Tectonophysics*, v. 273, p. 31–56.
- Herren, E., 1987, Zaskar shear zone: Northeast-southwest extension within the Higher Himalayas (Ladakh, India): *Geology*, v. 15, p. 409–413.
- Hodges, K., Bowring, S., Davidek, K., Hawkins, D., and Krol, M., 1998, Evidence for rapid displacement on Himalayan normal faults and the importance of tectonic denudation in the evolution of mountain ranges: *Geology*, v. 26, p. 483–486.
- Hodges, K.V., and Spear, F.S., 1982, Geothermometry, geobarometry and the Al_2SiO_5 triple point at Mt. Moosilauke, New Hampshire: *American Mineralogist*, v. 67, p. 1118–1134.
- Holland, T., Baker, J., and Powell, R., 1998, Mixing properties and activity-composition and relationships of chlorites in the system $\text{MgO-FeO-Al}_2\text{O}_3\text{-SiO}_2\text{-H}_2\text{O}$: *European Journal of Mineralogy*, v. 10, p. 395–406.
- Holland, T.J.B., and Powell, R., 1998, An internally consistent thermodynamic data set for phases of petrologic interest: *Journal of Metamorphic Geology*, v. 16, p. 309–343.
- Horton, F., and Leech, M.L., 2013, Age and origin of granites in the Karakoram shear zone and Greater Himalaya Sequence, NW India: *Lithosphere*, v. 5, p. 300–320, doi: 10.1130/L213.1.
- Inger, S., 1998, Timing of an extensional detachment during convergent orogeny: New Rb-Sr geochronological data from the Zaskar shear zone, northwestern Himalaya: *Geology*, v. 26, p. 223, doi: 10.1130/0091-7613(1998)026<0223:TOAEDD>2.3.CO;2.

- Ireland, T.R., and Williams, I.S., 2003, Considerations in Zircon Geochronology by SIMS: Reviews in Mineralogy and Geochemistry, Hanchar, J.M. and Hoskin, W.O., editors, v. 53, no. 215-241.
- Jamieson, R.A., Beaumont, C., Medvedev, S., and Nquyen, M.H., 2004, Crustal channel flows: 2. Numerical models with implications for metamorphism in the Himalayan-Tibetan orogen: *Journal of Geophysical Research*, v. 109, no. B6, doi: 10.1029/2003JB002811.
- Jamieson, R.A., Beaumont, C., Nguyen, M.H., and Grujic, D., 2006, Provenance of the Greater Himalayan Sequence and associated rocks: predictions of channel flow models: Geological Society, London, Special Publications, v. 268, p. 165.
- Jessup, M.J., Law, R.D., Searle, M.P., and Hubbard, M.S., 2006, Structural evolution and vorticity of flow during extrusion and exhumation of the Greater Himalayan Slab, Mount Everest Massif, Tibet/Nepal: implications for orogen-scale flow partitioning: Geological Society, London, Special Publications, v. 268, p. 379.
- Kohn, M.J., 2013, Himalayan Metamorphism and Its Tectonic Implications: *Annual Review of Earth and Planetary Sciences*, v. 42, p. 140307200240001, doi: 10.1146/annurev-earth-060313-055005.
- Kohn, M.J., 2008, P-T-t data from central Nepal support critical taper and repudiate large-scale channel flow of the Greater Himalayan Sequence: *Geological Society of America Bulletin*, v. 120, p. 259–273, doi: 10.1130/B26252.1.
- Kundig, R., 1989, Domal structures and high-grade metamorphism in the Higher Himalayan Crystalline, Zaskar Region, north-west Himalaya, India: *Journal of Metamorphic Geology*, v. 7, p. 43–55.
- Law, R.D., Jessup, M.J., Searle, M.P., Francis, M.K., Waters, D.J., and Cottle, J.M., 2011, Telescoping of isotherms beneath the South Tibetan Detachment System, Mount Everest Massif: *Journal of Structural Geology*, v. 33, p. 1569–1594, doi: 10.1016/j.jsg.2011.09.004.
- Leech, M., Singh, S., Jain, A., Klempner, S., and Manickavasagam, R., 2005, The onset of India–Asia continental collision: Early, steep subduction required by the timing of UHP metamorphism in the western Himalaya:

- Earth and Planetary Science Letters, v. 234, p. 83–97, doi: 10.1016/j.epsl.2005.02.038.
- Leloup, P.H., Mahéo, G., Arnaud, N., Kali, E., Boutonnet, E., Liu, D., Xiaohan, L., and Haibing, L., 2010, The South Tibet detachment shear zone in the Dinggye area Time constraints on extrusion models of the Himalayas: Earth and Planetary Science Letters, v. 292, p. 1–16, doi: 10.1016/j.epsl.2009.12.035.
- Lister, G.S., and Snoke, A.W., 1984, S-C Mylonites: Journal of Structural Geology, v. 6, p. 617–634.
- Ludwig, K.R., 2003, Isoplot (3.41d), a geochronological toolkit for Excel, Berkeley Geochronology Center Special Publication No. 4.
- Ludwig, K.R., 2009, Squid 2, A user manual, Berkeley Geochronology Center Special Publication No. 5.
- Mainprice, D., Bouchez, J.-L., Blumenfeld, P., and Tubià, J.M., 1986, Dominant c slip in naturally deformed quartz: Implications for dramatic plastic softening at high temperature: Geology, v. 14, p. 819, doi: 10.1130/0091-7613(1986)14<819:DCSIND>2.0.CO;2.
- Nábělek, P.I., and Nábělek, J.L., 2014, Thermal characteristics of the Main Himalaya Thrust and the Indian lower crust with implications for crustal rheology and partial melting in the Himalaya orogen: Earth and Planetary Science Letters, v. 395, p. 116–123, doi: 10.1016/j.epsl.2014.03.026.
- Nelson, K.D., Zhao, W., Brown, L.D., Kuo, J., Che, J., Liu, X., Klemperer, S.L., Makovsky, Y., Meissner, R., and Mechie, J., 1996, Partially molten middle crust beneath southern Tibet: Synthesis of project INDEPTH results: Science, v. 274, p. 1684–1688.
- Noble, S.R., and Searle, M.P., 1995, Age of crustal melting and leucogranite formation from U-Pb zircon and monazite dating in the western Himalaya, Zaskar, India: Geology, v. 23, p. 1135, doi: 10.1130/0091-7613(1995)023<1135:AOCMAL>2.3.CO;2.
- Pognante, U., Castelli, D., Benna, P., Genovese, G., Oberli, F., Meier, M., and Tonarini, S., 1990, The crystalline units of the High Himalayas in the Lahul, Zaskar region (northwest India): metamorphic, tectonic history and

- geochronology of the collided and imbricated Indian plate: *Geological Magazine*, v. 127, p. 101–116.
- Rosenberg, C.L., and Handy, M.R., 2005, Experimental deformation of partially melted granite revisited: implications for the continental crust: *Journal of Metamorphic Geology*, v. 23, p. 19–28, doi: 10.1111/j.1525-1314.2005.00555.x.
- Sachan, H.K., Kohn, M.J., Saxena, A., and Corrie, S.L., 2010, The Malari leucogranite, Garhwal Himalaya, northern India: Chemistry, age, and tectonic implications: *Geological Society of America Bulletin*, v. 122, p. 1865–1876.
- Schmid, S.M., and Casey, M., 1986, Complete fabric analysis of some commonly observed quartz c-axis patterns: *Geophysical Monograph Series*, v. 36, p. 263–286.
- Schmidt, N.H., and Olesen, N.O., 1989, Computer-aided determination of crystal-lattice orientation from electron channeling patterns in the SEM: *Canadian Mineralogist*, v. 27, p. 15–22.
- Searle, M.P., 1986, Structural evolution and sequence of thrusting in the High Himalayan, Tibetan—Tethys and Indus suture zones of Zaskar and Ladakh, Western Himalaya: *Journal of Structural Geology*, v. 8, p. 923–936.
- Searle, M.P., Law, R.D., and Jessup, M.J., 2006, Crustal structure, restoration and evolution of the Greater Himalaya in Nepal-South Tibet: implications for channel flow and ductile extrusion of the middle crust: *Geological Society, London, Special Publications*, v. 268, p. 355.
- Searle, M.P., and Rex, A.J., 1989, Thermal model for the Zaskar Himalaya: *Journal of Metamorphic Geology*, v. 7, p. 127–134.
- Searle, M.P., Simpson, R.L., Law, R.D., Parrish, R.R., and Waters, D.J., 2003, The structural geometry, metamorphic and magmatic evolution of the Everest massif, High Himalaya of Nepal–South Tibet: *Journal of the Geological Society*, v. 160, p. 345–366.
- Searle, M.P., Waters, D.J., Dransfield, M.W., Stephenson, B.J., Walker, C.B., Walker, J.D., and Rex, D.C., 1999, Thermal and mechanical models for the structural and metamorphic evolution of the Zaskar High Himalaya:

- Geological Society, London, Special Publications, v. 164, p. 139–156, doi: 10.1144/GSL.SP.1999.164.01.08.
- Sorkhabi, R.B., Jain, A.K., Itaya, T., Fukui, S., Lal, N., and Kumar, A., 1997, Cooling age record of domal uplift in the core of the Higher Himalayan Crystallines (HHC), southwest Zaskar, India: *Proceedings of the Indian Academy of Sciences-Earth and Planetary Sciences*, v. 106, p. 169–179.
- Stacey, J.S., and Kramers, J.D., 1975, Approximation of terrestrial lead isotope evolution by a two-stage model: *Earth and Planetary Science Letters*, v. 26, p. 207–221.
- Stipp, M., and Kunze, K., 2008, Dynamic recrystallization near the brittle-plastic transition in naturally and experimentally deformed quartz aggregates: *Tectonophysics*, v. 448, p. 77–97, doi: 10.1016/j.tecto.2007.11.041.
- Stipp, M., Stunitz, H., Heilbronner, R., and Schmid, S.M., 2002a, Dynamic recrystallization of quartz: correlation between natural and experimental conditions: *Geological Society, London, Special Publications*, v. 200, p. 171–190, doi: 10.1144/GSL.SP.2001.200.01.11.
- Stipp, M., Stunitz, H., Heilbronner, R., and Schmid, S.M., 2002b, The eastern Tonale fault zone: a 'natural laboratory' for crystal plastic deformation of quartz over a temperature range from 250 to 700°C: *Journal of Structural Geology*, v. 24, p. 1861–1884.
- Tullis, J., and Yund, R.A., 1977, Experimental deformation of dry Westerly granite: *Journal of Geophysical Research*, v. 82, p. 5705–5718.
- Vance, D., and Harris, N., 1999, Timing of prograde metamorphism in the Zaskar Himalaya: *Geology*, v. 27, no. 5, p. 395, doi: 10.1130/0091-7613(1999)027<0395:TOPMIT>2.3.CO;2.
- Vance, D., and Mahar, E., 1998, Pressure-temperature paths from P-T pseudosections and zoned garnets: potential, limitations and examples from the Zaskar Himalaya, NW India: *Contributions to Mineralogy and Petrology*, v. 132, p. 225–245.
- Walker, J.D., Martin, M.W., Bowring, S.A., Searle, M.P., Waters, D.J., and Hodges, K.V., 1999, Metamorphism, Melting, and Extension: Age Constraints from the High Himalayan Slab of Southeast Zaskar and

- Northwest Lahaul: *The Journal of Geology*, v. 107, p. 473–495, doi: 10.1086/314360.
- Walker, C.B., Searle, M.P., and Waters, D.J., 2001, An integrated tectonothermal model for the evolution of the High Himalaya in western Zaskar with constraints from thermobarometry and metamorphic modeling: *Tectonics*, v. 20, p. 810–833.
- White, S., 1977, Geological significance of recovery and recrystallization processes in quartz: *Tectonophysics*, v. 39, p. 143–170.
- White, R., Powell, R., Holland, T., and Worley, 2000, The effect of TiO_2 and Fe_2O_3 on metapelitic assemblages at greenschist and amphibolite facies conditions: mineral equilibria calculations in the system $\text{K}_2\text{O}-\text{FeO}-\text{MgO}-\text{Al}_2\text{O}_3-\text{SiO}_2-\text{H}_2\text{O}-\text{TiO}_2-\text{Fe}_2\text{O}_3$: *Journal of Metamorphic Geology*, v. 18, p. 497–511.
- Willett, S.D., 1999, Rheological dependence of extension in wedge models of convergent orogens: *Tectonophysics*, v. 305, p. 419–435.
- Williams, I.S., 1997, U-Th-Pb geochronology by ion microprobe: not just ages but histories: *Society of Economic Geologists Review*, v. 7, p. 1–35.
- Wobus, C.W., Hodges, K.V., and Whipple, K.X., 2003, Has focused denudation sustained active thrusting at the Himalayan topographic front?: *Geology*, v. 31, p. 861, doi: 10.1130/G19730.1.
- Zuluaga, C.A., Stowell, H.H., and Tinkham, D.K., 2005, The effect of zoned garnet on metapelite pseudosection topology and calculated metamorphic P-T paths: *American*, v. 90, p. 1619–1628.

Figure Captions

Figure 1. Geologic map of the Zaskar area in NW India showing the major structural features and geologic units. Cross-section A-B shows the structural relation between these units. The sampling area for this study is in Malung Tokpo, NW of Padum. Poles to foliation and stretching lineation from Malung Tokpo are plotted on an equal area stereoplot. Location of samples included in the U-Pb analyses collected outside of Malung Tokpo are marked. GHS, Greater Himalayan Sequence; IYSZ, Indus Yarlung Suture Zone; LB, Ladakh Batholith; LHS, Lesser Himalayan Sequence; MCT, Main Central Thrust; THS, Tethyan Himalayan Sequence; ZSZ, Zaskar Shear Zone. (Modified from Horton and Leech, 2013).

Figure 2. Google Earth image of Malung Tokpo with sample locations and structural data. Zaskar Shear Zone trends E-W with the Greater Himalayan sequence to the south and the Tethyan Himalayan sequence to the north. Inset is a view of the shear zone with the sample numbers and locations for a closer perspective of their relative positions within the shear zone. Structural data is plotted as strike and dip of foliation with trend and plunge of elongated grains on the foliation plane indicative of top-to-the-NE movement.

Figure 3. Plot of core to rim molar weight percent of the Alm, Sps, Prp, and Grs components of the garnet chemistry in ZH-12. Data is based on a 5-point representative sampling transect. Plot shows Mg-rich cores, and Fe- and Mn-rich rims.

Figure 4. (a) Plot of the uncorrected $^{206}\text{Pb}/^{238}\text{U}$ values for ZH-28 zircon. This sample was chosen because of low measured common ^{206}Pb . The plot shows progressive sampling through the rim with low measured $^{206}\text{Pb}/^{238}\text{U}$, corresponding to Miocene ages, to the core, which generated Cambrian

ages when averaged with the Miocene ages. The Cambrian ages are not representative of an age of growth since they are an average of two populations and likely included an inheritance age signature. The increase in apparent age attributed to depth profiling through thin ($\sim 2 \mu\text{m}$) rims during analysis. (b) A schematic diagram of a zircon grain and the pit formed during sampling that cuts through the rim to the core of the grain. (c) CL image of ZH28 zircon grain with sampling location marked by dark spot on the surface.

Figure 5. Outcrop scale view of the Zanskar Shear Zone in Malung Tokpo. Major units labeled GHS (Greater Himalayan Sequence) and THS (Tethyan Himalayan Sequence). All images are oriented with a top-to-NE shear sense. (a) Feldspathic megacryst exhibiting top-to-NE shearing. Rock hammer for scale. (b) In situ shear band and feldspar sigma-clast development indicative of top-to-the-NE movement. Sharpie for scale. (c) Large-scale folding of pre- and syntectonic leucogranites. Ted for scale. (d) Leucogranite dike (ZH-9; solid black outline) cross cutting deformed leucogranite (small dashes) intrusion and normal-sense offset (large dashes). Rock hammer for scale. Photomicrographs of samples ZH-16, ZH-22, and ZH-3 illustrate the progressive degree of mylonitization relative to distance from ZSZ. The dominant mineral assemblage shown is $\text{Pl} + \text{Qz} + \text{Bt} \pm \text{Ms} \pm \text{Sil}(\text{Fi}) \pm \text{Kfs}$.

Figure 6. Photomicrographs of metamorphic assemblages and textures in schists and orthogneisses from Malung Tokpo. All photomicrographs are oriented top-up with NE to the right, with the exception of ZH-12 which is not oriented. (a) Myrmekite intergrowths of Pl and Qz with a Crd corona around Ky in ZH-12. (b) Crd coronae around Ky grains in a Bt and Pl matrix in ZH-12. (c) Large (2mm) Grt porphyroblast in ZH-12 that exhibits

multiple growth phases with Bt + Crd grains included in Grt rims. (d) Extensional microfractures in Grt exhibiting top-to-the-NE brittle deformation that does not continue into the rock matrix in ZH-14. Retrograde Chl exists on S_1 and S_2 foliation planes. Inset shows similar retrograde replacement of Grt with Bt + Chl in ZH-24. (e) St grains sheared into alignment with S_1 and S_2 , which are both sympathetic to the regional top-to-the-NE shearing. Ms and Bt form within both foliation planes in ZH-15. (f) Microboudinaged St grain with Sil growing in the necks of the boudins. St is aligned parallel with the foliation. (g) Sheared and rotated Qz ribbon with Ms-rich foliation wrapping around the folded Qz ribbon. The asymmetry shown indicates top-to-the-NE shearing in ZH-24. (h) Sil(Fi) growing after Bt in ZH-24.

Figure 7. Pseudosections for metapelites ZH-14, ZH-15, ZH-12, and ZH-24 from the GHS in Malung Tokpo. Pseudosections were calculated in the MnNCKFMASHTO system with saturated H_2O and SiO_2 and constrained by their XRF whole-rock data. Variance is illustrated by the gray-scale shading in each field with variance increasing with darker shades of gray/black. Mineral abbreviations are after Whitney and Evans (2010). White ellipses represent the area of intersection of the garnet isopleths for the Alm, Pyr-, Sps-, and Grs-components (see Appendix I). Green line shows the Fe-Mg exchange temperature calculation for Grt-Bt using Ferry and Spear (1978); the orange line shows Grt-Bt thermometry using Hodges and Spear (1982). The yellow arrows are proposed P-T paths. Pseudosection for ZH-12 is calculated based on whole-rock chemistry after garnet core chemistries were removed. See Appendix I for garnet isopleths plotted on all pseudosection fields.

Figure 8. Terra-Wasserberg concordia diagrams showing U-Pb SHRIMP data acquired for igneous zircons in ZH-9, ZH-25, and Z-4. Stacey-Kramer modeled line projected to $^{207}\text{Pb}/^{206}\text{Pb}=0.837$. Error associated with the discordant points on this line can be attributed to common Pb. Error ellipses are 2σ . Mean ages are calculated from ^{207}Pb -corrected $^{206}\text{Pb}/^{238}\text{U}$ ages (box heights represent 2σ error).

Figure 9. Terra-Wasserberg concordia diagrams showing U-Pb SHRIMP data acquired for metamorphic zircons from ZH-36, ZH-41, and Z-32. Stacey-Kramer modeled line projected to $^{207}\text{Pb}/^{206}\text{Pb}=0.837$. Error associated with the discordant points on this line can be attributed to common Pb. Error ellipses are 2σ . Light blue ellipses are included in weighted mean age estimates; magenta ellipses are not included in calculations because of large errors. Mean ages are calculated from ^{207}Pb -corrected $^{206}\text{Pb}/^{238}\text{U}$ ages (box heights represent 2σ error).

Figure 10. Illustration of a cross-sectional view of Malung Tokpo showing metamorphic isograds and sample locations (modified from Herren, 1987). The proposed location for the Ky-in isograd is represented by thick-dashed orange line. (a-i) Equal-area lower hemisphere plots of quartz $\langle c \rangle$ and $\langle a \rangle$ -axis ($\langle 0001 \rangle$ and $\{11-20\}$) CPOs. (h and i) Plots of isolated small grains and large grains in ZH-14 (h) and ZH-22 (i). The small grains in ZH-14 exhibit a 70° rotation from the large grains.

Figure 11. (a) Plot of compiled P-T paths for samples ZH-12, ZH-14, ZH-15, and ZH-24. Dashed lines indicate inferred P-T path based on a “normal” geothermal gradient. Different stages on the P-T paths are labeled 1-4 (see text). Geo/thermochronology results from U-Pb (Zrn) analyses in this study, U-Pb (Mzn) ages (Horton and Leech, 2013), Sm-Nd (Grt) ages

(Vance and Harris, 1999), preliminary $^{40}\text{Ar}/^{39}\text{Ar}$ ages for Ms and Bt, and apatite fission track (AFT) ages (Sorkhabi et al., 1997). Black crosses indicate errors of $\pm 50^\circ\text{C}$ and ± 1 kbar based on closure temperatures for thermochronometers and calculate pressures assuming a $37^\circ\text{C}/\text{km}$ geothermal gradient (Nábělek and Nábělek, 2014). Rough exhumation rates between peak metamorphism (U-Pb in Zrn) and initial cooling in upper crust ($^{40}\text{Ar}/^{39}\text{Ar}$ in Ms) and between initial cooling ($^{40}\text{Ar}/^{39}\text{Ar}$ in Ms) and exhumation (AFT) are labeled below the P-T curves. (b) Predicted channel flow and critical taper P-T and (c) T-t plots modified from Kohn (2008) and include a plot of this study's T-t history of the GHS in Zanskar.

Appendices

Appendix I. Pseudosections for samples ZH-14, ZH-15, ZH-24, and ZH-12 from the GHS in Malung Tokpo as in Figure 7. White ellipses represent the area of intersection of the garnet isopleths for the Alm, Pyr-, Sps-, and Grs-components. Isopleth range for ZH-14 is $\text{Alm}_{69-70}\text{Sps}_{11-13}\text{Grs}_8\text{Pyr}_{9-10}$, ZH-15 is $\text{Alm}_{69-72}\text{Sps}_{6-9}\text{Grs}_{10-15}\text{Pyr}_8$, ZH-24 is $\text{Alm}_{80-81}\text{Sps}_{5-8}\text{Grs}_{3-4}\text{Pyr}_{7-9}$, and ZH-12 is $\text{Alm}_{57-61}\text{Sps}_{8-15}\text{Grs}_{1-3}\text{Pyr}_{20-31}$. Isopleths are plotted on a 1% contour interval. Maximum values are dotted lines. Arrows in ellipses on ZH-24 and ZH-12 indicate the change in garnet core to rim values.

Appendix II. Table of SHRIMP-RG U-Pb analyses. Data are reduced to include three scans per grain. The data presented are those incorporated in the Terra-Wasserberg Concordia diagrams and weighted average plots.

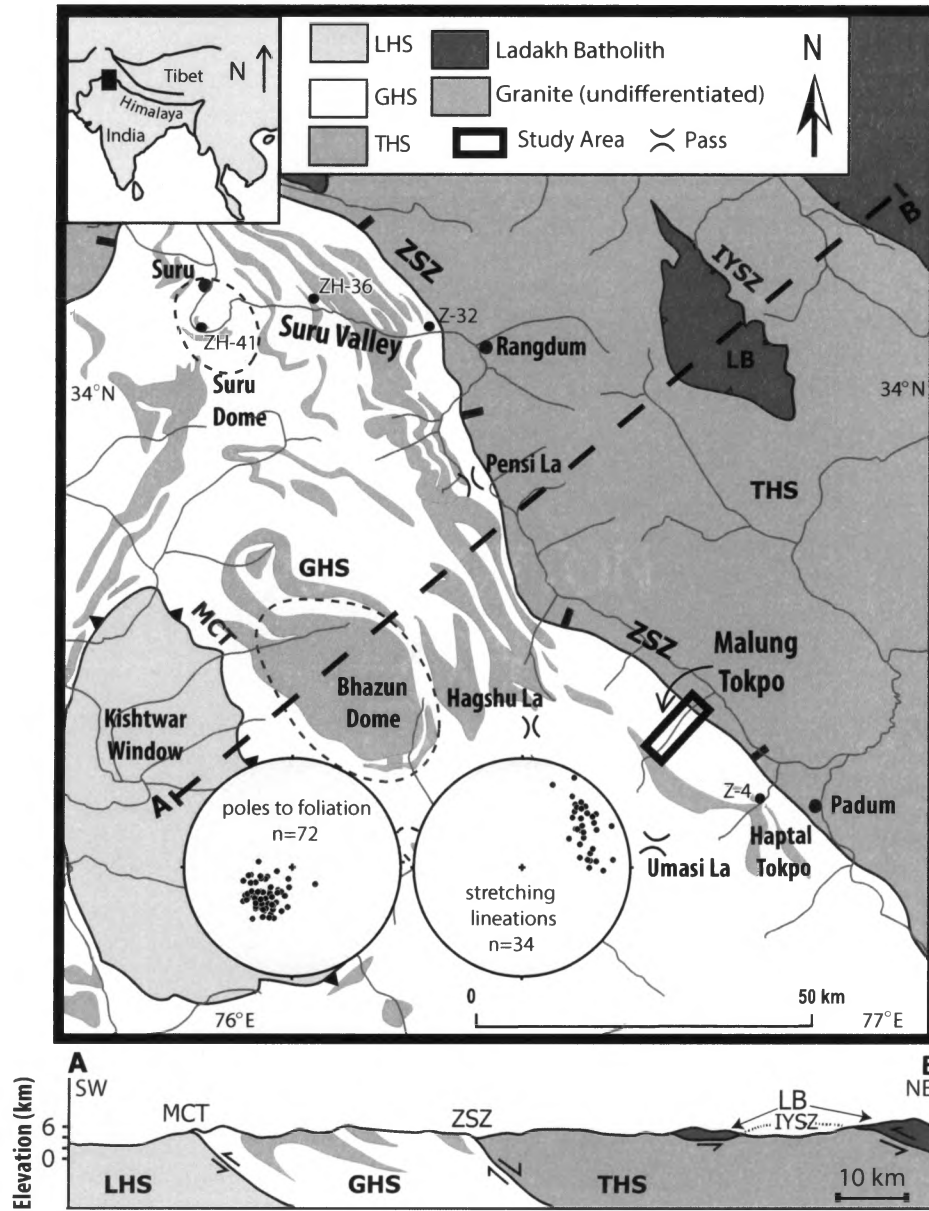


Figure 1

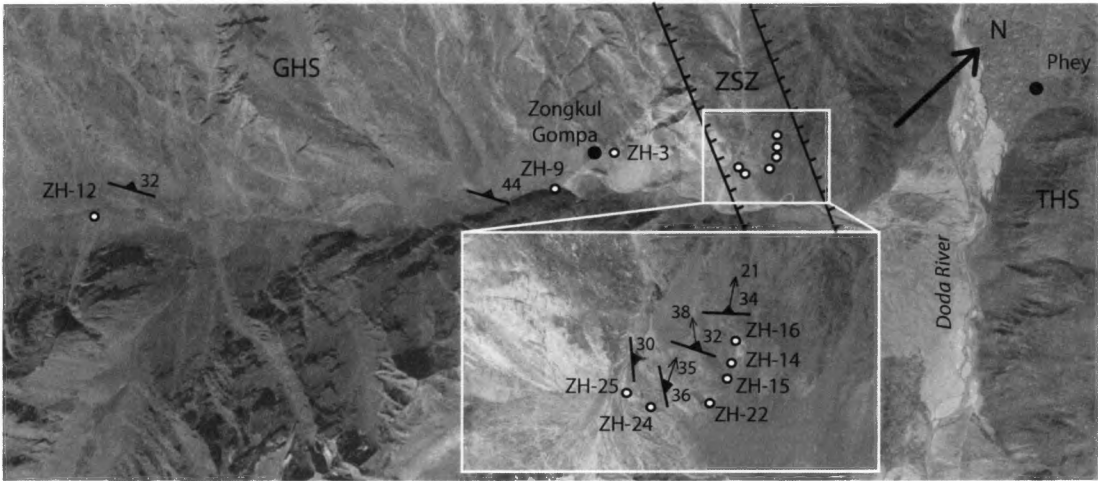


Figure 2

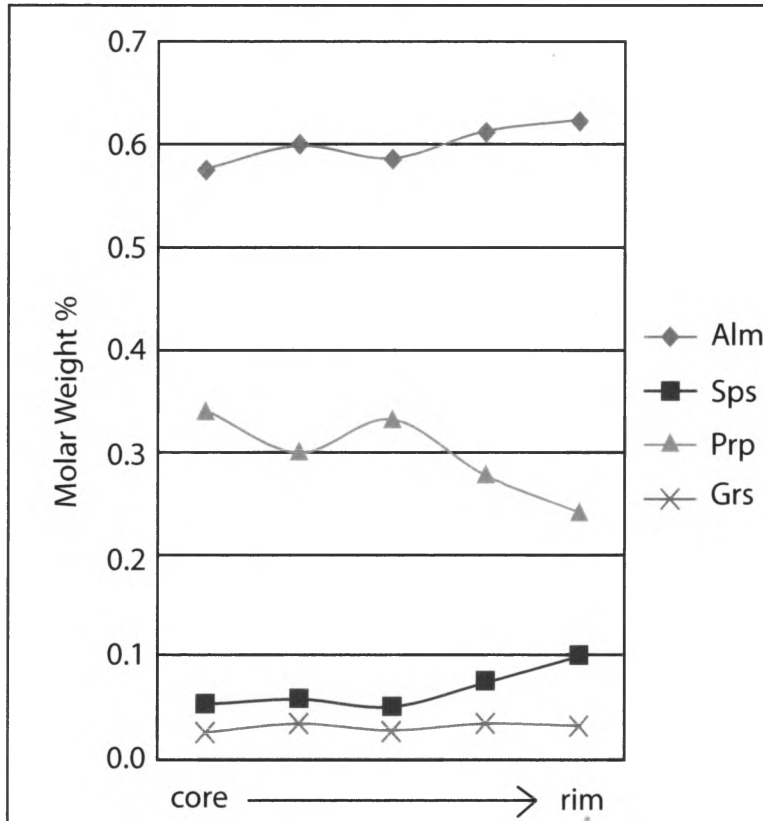


Figure 3

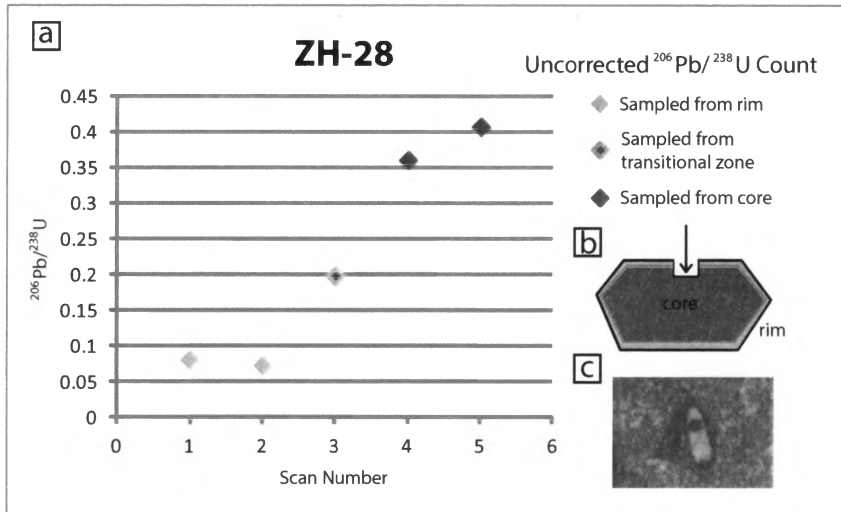


Figure 4

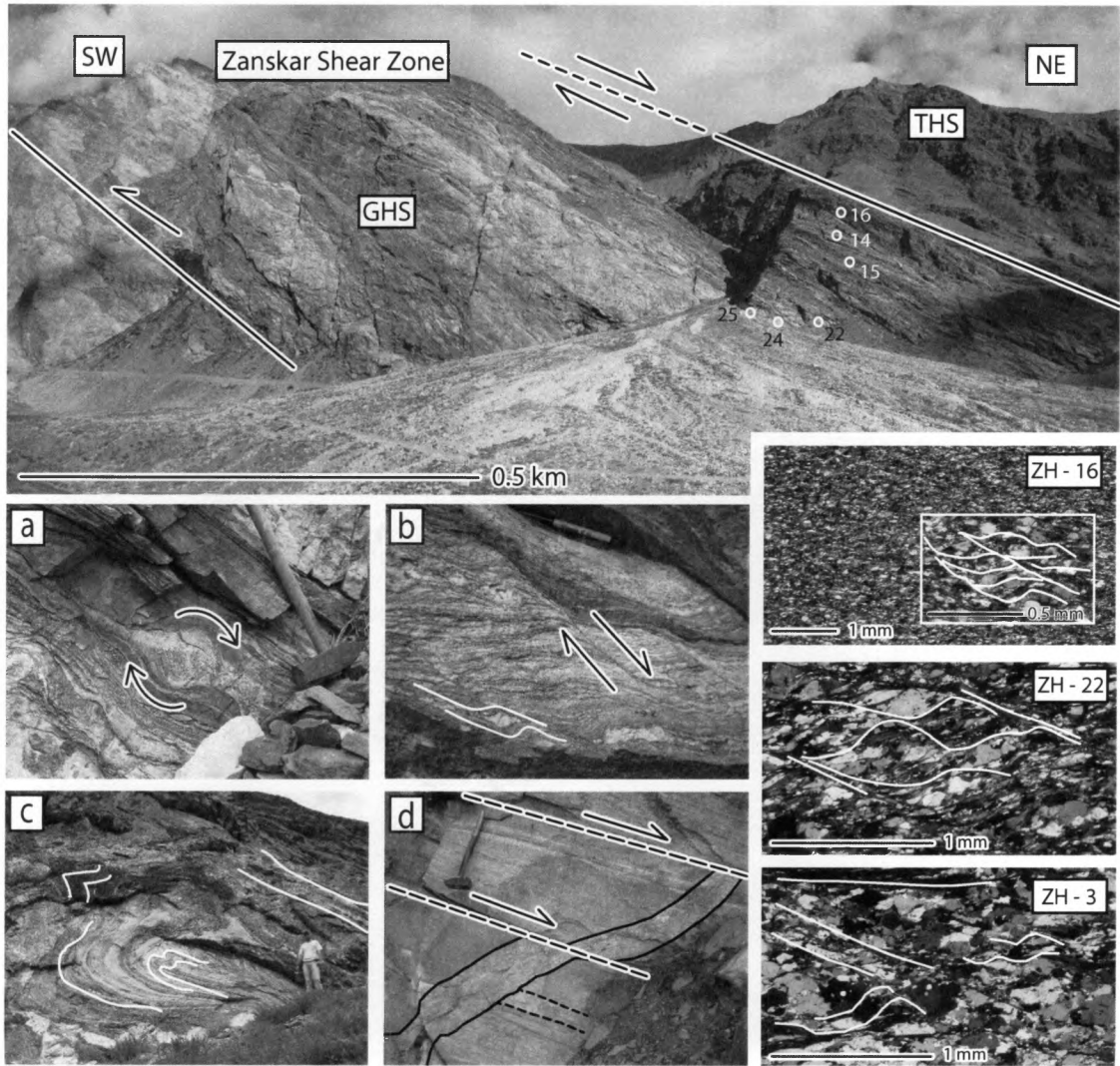


Figure 5

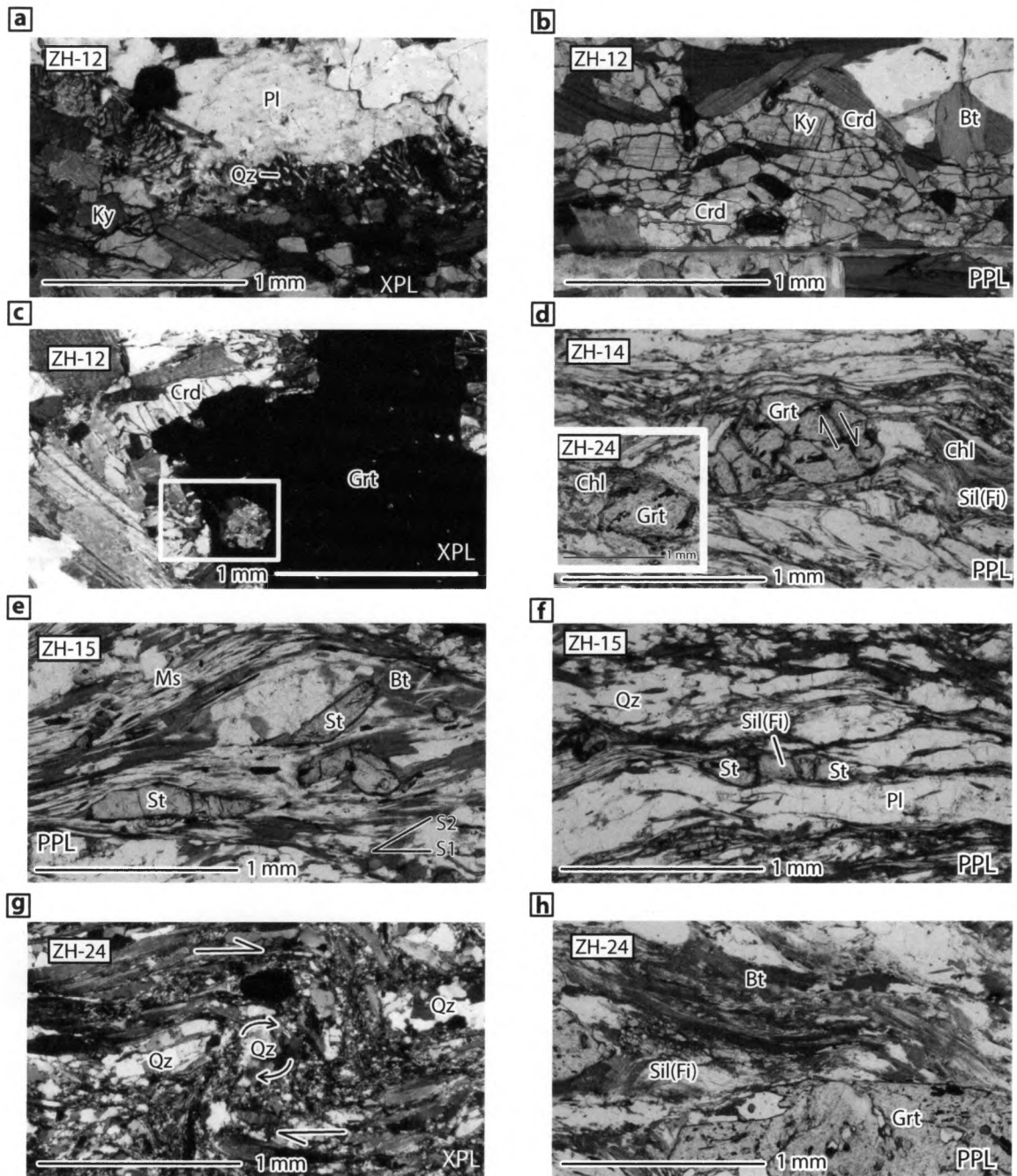


Figure 6

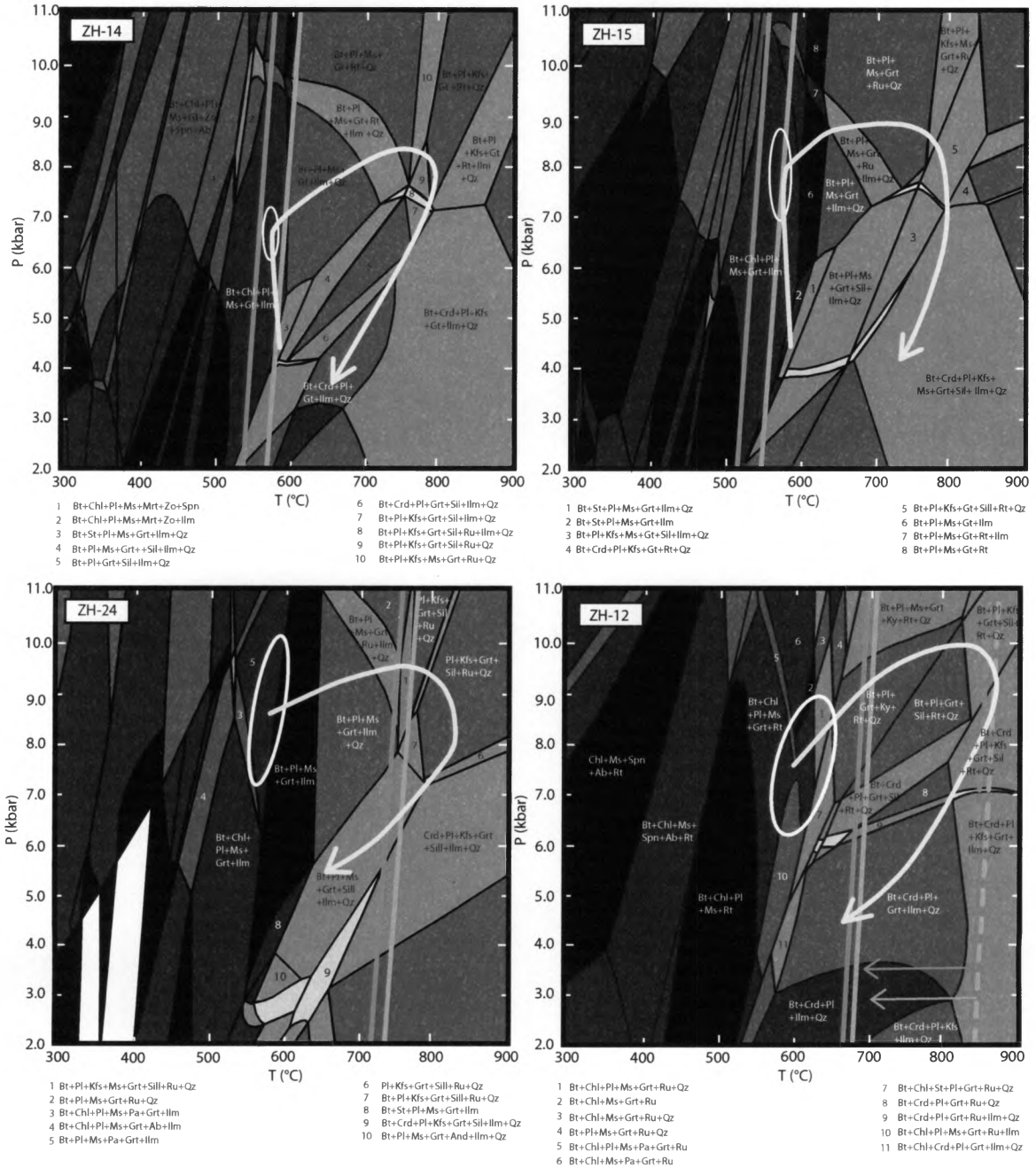


Figure 7

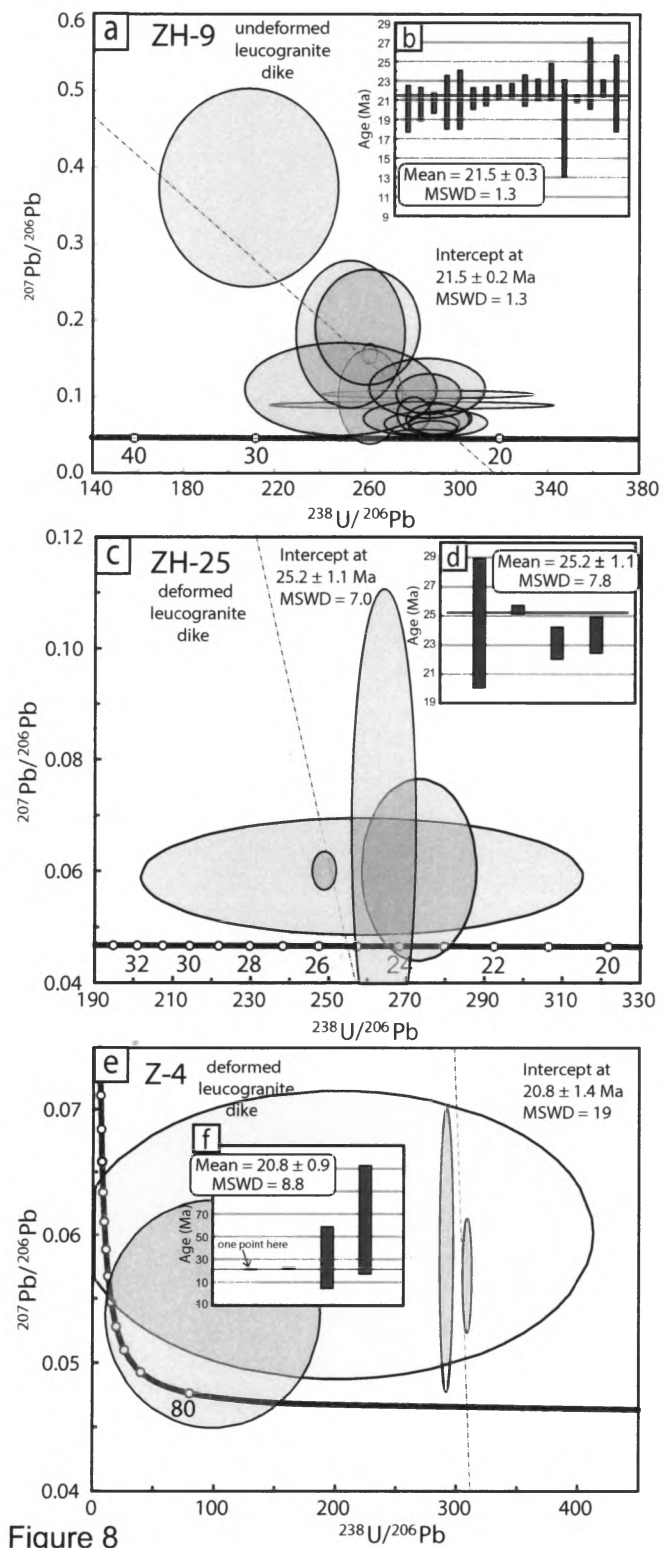


Figure 8

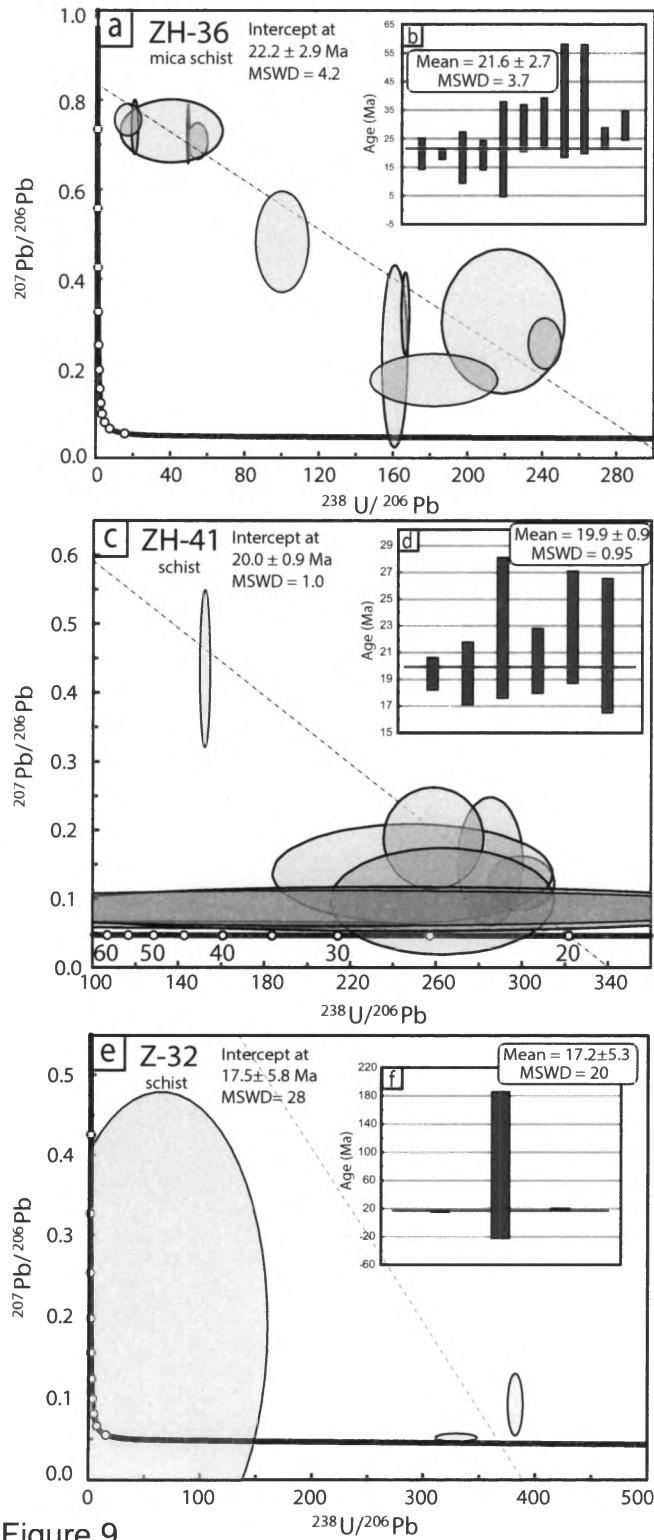


Figure 9

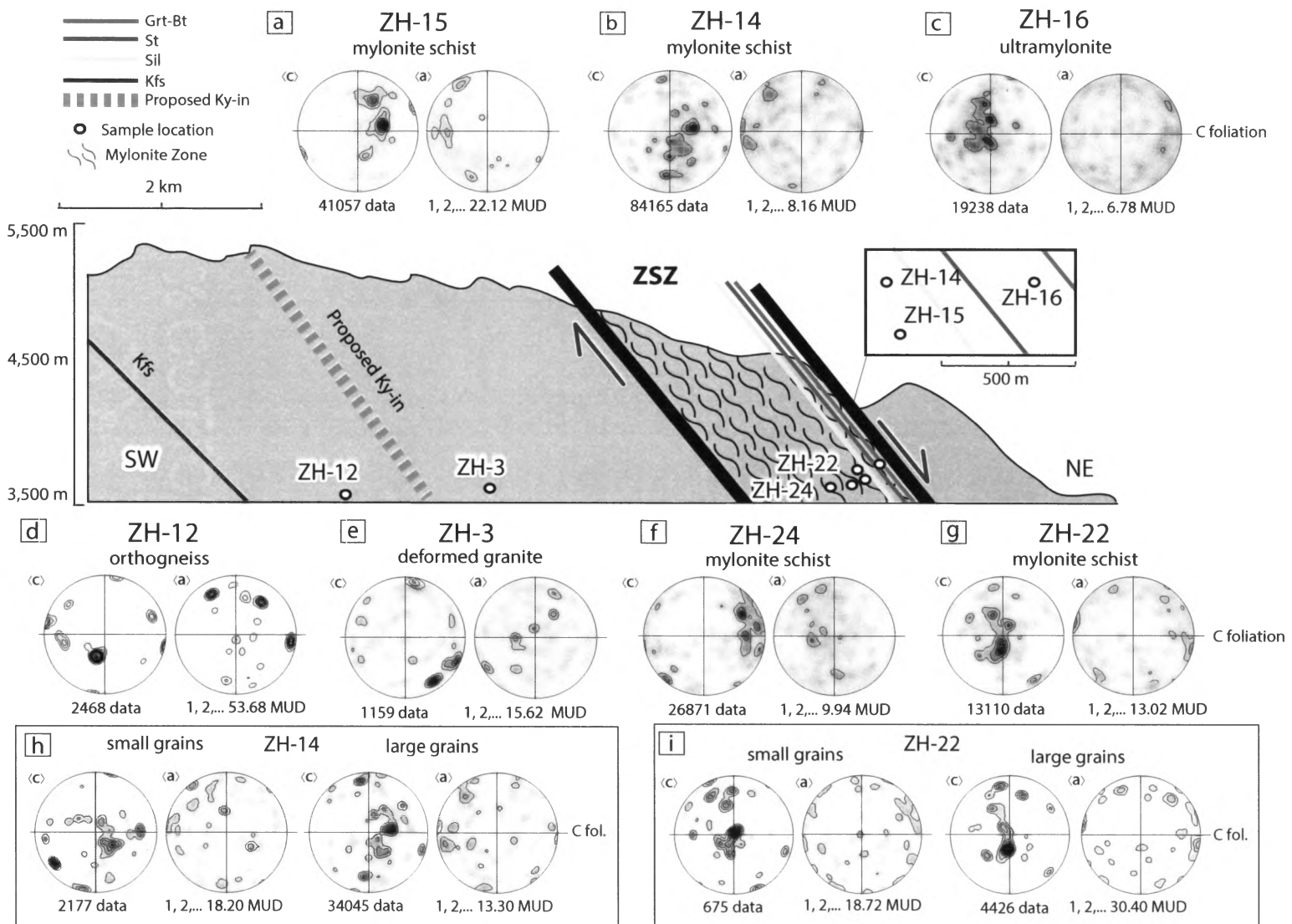


Figure 10

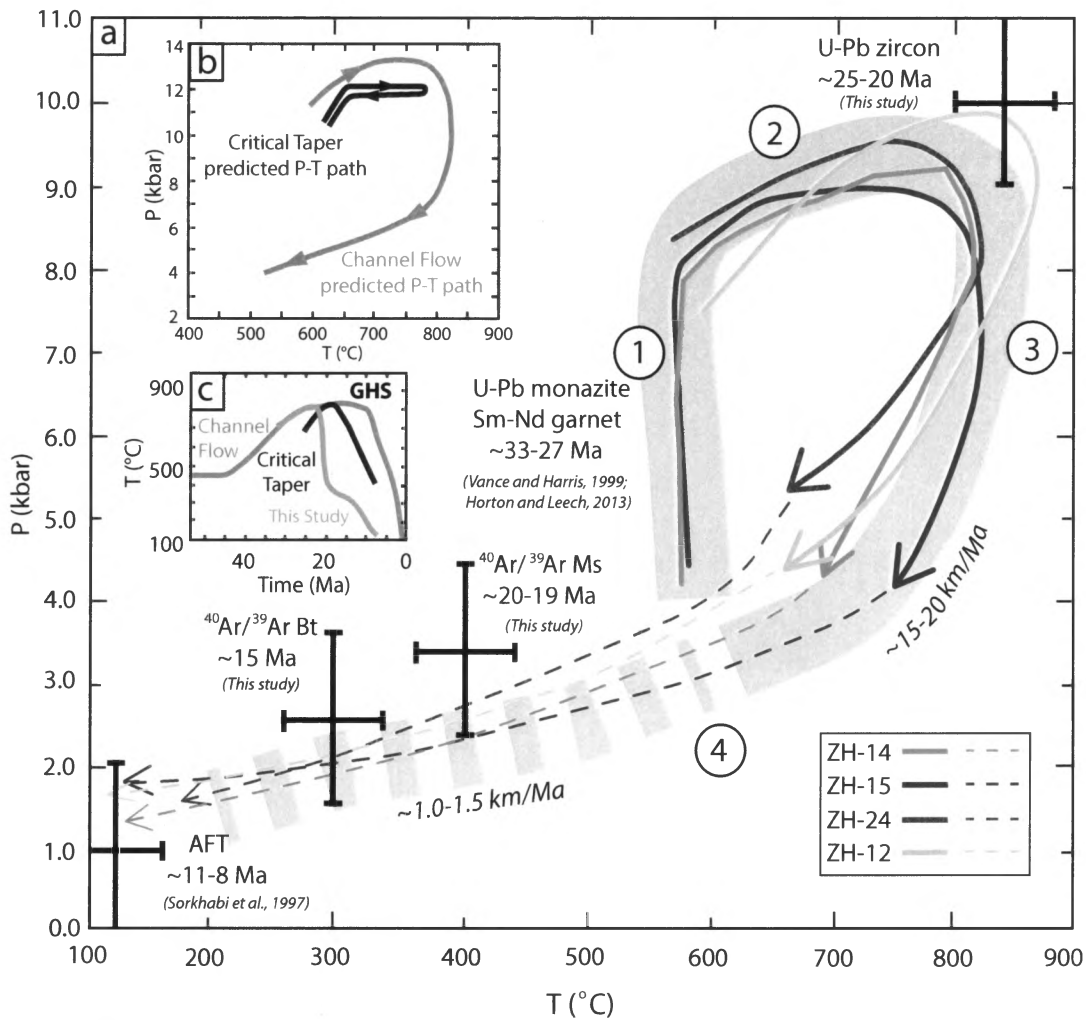


Figure 11

TABLE 1. SUMMARY OF ZANSKAR DATING

Age (Ma)	Rock Type	Method	Mineral	Zanskar Region	Source
8.1 ± 0.4	Migmatite	AFT	Ap	SE- Malung Tokpo	Sorkhabi et al. (1997)
11.0 ± 0.3	Gneiss	AFT	Ap	SE- Haptal Tokpo	Sorkhabi et al. (1997)
~15 Ma	GHS	Ar/Ar	Bt	Suru Valley	This Study
15.5 ± 0.1	GHS	Ar/Ar	Bt	Suru Valley	Searle et al.(1992)
20.5 ± 0.3	Schist	Ar/Ar	Bt	SE- Gumberanjan	Walker et al. (1999)
~20-19	GHS	Ar/Ar	Ms	Suru Valley	This Study
18.0 ± 1.0	Leucogranite	Ar/Ar	Ms	Suru Valley	Searle et al.(1992)
19.8 ± 0.1	Undefm Leucogranite	Ar/Ar	Ms	SE- Gumberanjan	Dèzes et al. (1999)
20.18 ± 0.54	Leucogranite	Ar/Ar	Ms	SE- Gumberanjan	Walker et al. (1999)
23-22 ± 1.0	Garnet mica schist	Ar/Ar	Ms	NE- Padum	Searle et al.(1992)
13.5 ± 0.5	Gneiss	Rb-Sr	Bt	NW	Honegger et al. (1982)
16.3-15.4	GHS	Rb-Sr	Bt	NW - Sanku	Inger (1998)
16.4-12.8	GHS	Rb-Sr	Bt	Suru Dome	Inger (1998)
18.2 ± 0.4	GHS	Rb-Sr	Ms	SE- Haptal Tokpo	Inger (1998)
31-28	GHS	Sm-Nd	Grt	Suru Valley-Suru Dome	Vance and Harris (1999)
33-31	GHS	Sm-Nd	Grt	Suru Valley-Suru Dome	Vance and Harris (1999)
21.4 ± 0.1	Leucogranite	U-Pb	Zrn	SE- Gumberanjan	Walker et al. (1999)
27.3 ± 1.2	Schist	U-Th-Pb	Mzn	Suru Valley	Horton and Leech (2013)
23-21.5	Undefm Leucogranite	U-Pb	Mzn	SE- Gumberanjan	Finch et al (2014)
24.0 ± 0.25	Defm Leucogranite	U-Pb	Mzn	SE- Malung Tokpo	Finch et al (2014)
22.9±0.9-18.1±2	Undefm Leucogranite	U-Pb	Zrn	SE- Malung Tokpo	This Study
25.2 ± 1.1	Defm Leucogranite	U-Pb	Zrn	SE- Malung Tokpo	This Study
20.0 ± 0.9	Mica schist	U-Pb	Zrn	Suru Valley	This Study
21.5 ± 2.7	Mica schist	U-Pb	Zrn	Suru Valley	This Study

Note: Undefm-undeformed; Defm-deformed; AFT- Apatite fission track; Mineral abbreviations after Whitney and Evans (2010).

TABLE 2. SUMMARY OF SAMPLE DESCRIPTIONS AND CORRESPONDING RESULTS

Sample	Lat/Lon	Distance from ZSZ (km)	Rock Type	Min Assemblage	Qz Slip System(s)	P-T Stability	U-Pb Age
ZSZ	N 33° 35.244', E 76° 41.702'	±3 m resolution		Identified in thin section or hand sample		P (kbar) T(°C)	Wt Avg (Ma)
ZH-16	N 33° 35.239', E 76° 41.700'	0.02	Ultramylonite	Qz+Pl+Kfs+Bt+Ms	rhomb <a>	-	-
ZH-14	N 33°35.189', E 76°41.779'	0.07	Mylonitized mica Schist	Qz+Pl+Kfs+Bt+Ms+Grt+ Sil(Fi)+Ilm+Rt+St+Tur	prism <a>, c-slip	5-8 kbar 500-800 °C	-
ZH-15	N 33° 35.201', E 76° 41.766'	0.07	Mylonitized mica Schist	Qz+Pl+Kfs+Bt+Ms+Grt+ Sil(Fi)+St+Ilm+Rt	prism <a>	5.5-9 kbar 550-800 °C	-
ZH-22	N 33° 35.046', E 76° 41.7052'	0.40	Qfp orthogneiss	Qz+Pl+Kfs+Bt+Ms+Grt	rhomb <a>, prism <a>	-	-
ZH-24	N 33° 35.0157', E 76° 41.6617'	0.48	Qfp orthogneiss	Qz+Pl+Kfs+Ms+Bt+Grt+ Sil(Fi)+Chl+Ilm+Tur	c-slip	6-10 kbar 400-850 °C	-
ZH-25	N 33° 35.0047', E 76° 41.6327'	0.52	Defm leucogranite	Qz+Pl+Kfs+Ms+Hbl+Bt	-	-	25.2 ± 1.1
ZH-3	N 33° 34.5833', E 76° 40.9500'	1.75	Defm leucogranite	Qz+Pl+Kfs+Sil(Fi)+Ms+ Bt+Grt+Ilm	c-slip	-	-
ZH-9	N 33° 33.9667', E 76° 40.7333'	2.91	Undefm leucogranite	Qz+Pl+Kfs+Bt+Ms+Tur	-	-	21.5 ± 0.3
ZH-12	N 33°32.56', E 76°39.364'	6.17	Qfp orthogneiss	Qz+Pl+Kfs+Bt+Grt+Crd+ Ky+Ilm	no pattern	5.5-9 kbar 600-850 °C	-
Location							
ZH-36	N 34°4.939', E 76°5.388'	Suru Valley - W Rangdum	Mica Schist	-	-	-	21.6 ± 2.7
ZH-41	N°34 3.225', E 75°57.238'	Suru Dome	Mica Schist	-	-	-	19.9 ± 0.9
Z-4	N 33°26.992', E 76°47.005'	Haptal Takpo	Defm Leucogranite	-	-	-	20.8 ± 0.9
Z-32	N 34°3.235', E 76°17.572'	Nun-Kun Valley	Garnet Schist	-	-	-	17.2 ± 5.3

Note: Dominant slip systems present in recrystallized quartz grains as determined by EBSD crystallographic mapping, P-T path direction and P-T stability range as determined by pseudosection modeling and Grt-Bt thermometry, and U-Pb Stacey-Kramer model age. Samples at the bottom of the table are from areas surrounding Malung Takpo and are included for their U-Pb results for zircon. Qfp- quartzofeldspathic; Defm- deformed; Undefm- undeformed; CW- clockwise; CCW- counter clockwise; Wt Avg-weighted average; Mineral abbreviations after Whitney and Evans (2010).

TABLE 3. SUMMARY OF XRF BULK ROCK ANALYSES

Unnormalized Major Elements (Weight %):				
	ZH-12	ZH-14R	ZH-15	ZH-24
SiO₂	57.253	66.312	63.416	64.335
TiO₂	0.911	0.852	0.792	0.666
Al₂O₃	16.689	15.397	17.118	18.333
FeO*	8.867	5.894	6.695	6.007
MnO	0.232	0.095	0.097	0.133
MgO	6.984	2.447	2.615	1.325
CaO	0.483	2.244	1.610	0.540
Na₂O	1.281	2.981	2.237	1.790
K₂O	3.644	2.494	3.311	3.936
P₂O₅	0.116	0.155	0.152	0.078
Sum	96.460	98.870	98.040	97.142
LOI (%)	2.958	1.080	1.479	1.762
Unnormalized Trace Elements (ppm)				
Ni	19	27	51	28
Cr	80	94	104	52
Sc	17	15	17	19
V	107	102	109	87
Ba	664	515	582	581
Rb	168	130	175	237
Sr	50	175	149	97
Zr	260	322	192	194
Y	32	42	35	38
Nb	12.5	16.0	16.4	14.1
Ga	23	21	23	24
Cu	56	27	29	7
Zn	193	70	105	117
Pb	35	28	30	22
La	44	55	48	40
Ce	88	112	94	83
Th	16	25	20	15
Nd	39	48	38	38
U	3	4	4	3
Cs	12	28	15	65

Note: Total Fe expressed at FeO. LOI - Loss on ignition

TABLE 4. SUMMARY OF MICROPROBE GRT AND BT CHEMISTIES & GRT-BT THERMOMETRY

Garnet apfu								
Sample	ZH14		ZH15		ZH24		ZH12	
	rim	core	rim	core	rim	core	rim	core
Fe	2.121	2.150	2.197	2.137	2.465	2.471	1.862	1.749
Mn	0.382	0.347	0.269	0.200	0.251	0.172	0.459	0.262
Mg	0.295	0.308	0.270	0.252	0.213	0.282	0.638	0.965
Ca	0.249	0.249	0.305	0.473	0.109	0.130	0.091	0.082

Biotite apfu								
	matrix	matrix	matrix	core	matrix	matrix	matrix	core
Al	1.844	1.843	1.838	1.866	2.143	1.840	1.716	1.127
Ti	0.083	0.102	0.100	0.083	0.123	0.159	0.069	0.182
Fe	1.425	1.324	1.389	1.446	1.361	1.696	0.991	1.116
Mn	0.014	0.011	0.012	0.010	0.008	0.013	0.015	0.015
Mg	1.230	1.173	1.105	1.076	0.555	0.698	1.701	1.618
Ca	0.002	0.001	0.004	0.005	0.000	0.000	0.000	0.000
K	0.881	0.935	0.972	0.966	0.927	0.935	0.940	0.999
Na	0.039	0.050	0.000	0.013	0.054	0.035	0.048	0.057
Alm	0.697	0.721	0.812	0.679	0.815	0.812	0.600	0.537
Prp	0.097	0.100	0.081	0.074	0.087	0.081	0.234	0.315
Sps	0.114	0.099	0.067	0.054	0.059	0.067	0.136	0.129
Grs	0.091	0.081	0.039	0.193	0.039	0.039	0.030	0.019

Grt-Bt Thermometry								
Ferry and Spear, 1978 (°C)								
P (kbar)	Grt rim-matrix Bt	Grt core-matrix Bt	Grt rim-matrix Bt	Grt core-Bt incl	Grt rim-matrix Bt	Grt core-matrix Bt	Grt rim-matrix Bt	Grt core-Bt incl
5.5	547.3	537.6	634.1	632.3	702.9	735.9	647.2	848.5
9.5	562.0	552.1	650.3	648.5	719.2	754.0	663.6	868.5

Hodges and Spear, 1982 (°C)								
P (kbar)	Grt rim-matrix Bt	Grt core-matrix Bt	Grt rim-matrix Bt	Grt core-Bt incl	Grt rim-matrix Bt	Grt core-matrix Bt	Grt rim-matrix Bt	Grt core-Bt incl
5.5	582.9	568.9	667.6	679.0	719.2	752.3	659.4	856.7
9.5	597.2	583.1	683.3	694.6	736.4	770.1	675.7	876.6

Note: Garnet compositions are average values. Temperatures are representative of rim-matrix and core-inclusion (incl) temperatures, or are both rim-matrix temperatures if only matrix biotite values are listed. 12 oxygens used for garnet and biotite.

APPENDIX II. SHRIMP-PR U-Pb ANALYSES OF ZIRCON

Spot Number	U (ppm)	Th (ppm)	²³² Th / ²³⁸ U	²⁰⁴ Pb / ²⁰⁶ Pb	Common ²⁰⁶ Pb (%)	²³⁸ U / ²⁰⁶ Pb	²⁰⁷ Pb / ²⁰⁶ Pb	²⁰⁶ Pb / ²³⁸ U Age (Ma)	1σ err
ZH9-1.1a	1892	24	0.013	0.0063	13.97	262	0.1569	21.2	0.2
ZH9-1.1b	4528	14	0.003		1.08	286.1	0.0551	22.3	0.4
ZH9-1.2	3850	57	0.015	0.0023	3.28	283	0.0725	22.0	0.8
ZH9-2.1	4650	11	0.003	0.0014	1.78	290	0.0605	21.8	0.3
ZH9-4.1a	3183	17	0.006	0.0047	8.22	287	0.1115	20.6	0.9
ZH9-4.1b	3703	38	0.011	0.0022	5.51	280	0.0900	21.7	2.0
ZH9-6.1	4377	36	0.009	0.0007	2.58	296	0.0669	21.2	0.5
ZH9-8.1	627	5	0.008	0.0198	41.46	208	0.3741	18.1	2.5
ZH9-9.1	4185	11	0.003	0.0046	7.31	287	0.1043	20.8	1.4
ZH9-10.1	4098	60	0.015	0.0036	6.92	262	0.1012	22.9	0.9
ZH9-12.1	3852	32	0.009	0.0011	3.14	292	0.0713	21.4	0.5
ZH9-15.1	2227	55	0.025	0.0028	2.44	285	0.0658	22.1	0.6
ZH9-16.1	3780	27	0.007	0.0054	8.14	249	0.1109	23.8	1.8
ZH9-17.1	2269	38	0.017	0.0056	7.37	287	0.1048	20.7	0.5
ZH9-21.1	1352	30	0.023	0.0101	18.51	261	0.1928	20.1	1.2
ZH9-22.1	3787	76	0.021	0.0022	4.03	281	0.0783	22.0	0.4
ZH9-23.1	1351	23	0.017	0.0070	17.24	253	0.1828	21.0	1.5
ZH25-1.1	7967	53	0.007	0.0016	1.72	248.8	0.0602	25.4	0.1
ZH25-2.1	7179	27	0.004	0.0014	1.59	258.4	0.0591	24.5	2.2
ZH25-3.1	7939	18	0.002	0.0012	2.73	264	0.0681	23.7	0.6
ZH25-5.1	10004	26	0.003	0.0009	1.76	273	0.0604	23.1	0.5
ZH36-1.1	41	0	0.004	0.0408	86.64	40	0.7314	21.3	8.3
ZH36-5.1	78	0	0.005	0.0170	26.66	241	0.2572	19.6	0.8
ZH36-6.1	58	0	0.008	0.0188	22.98	161	0.2284	30.8	4.2
ZH36-7.1	56	1	0.013	0.0000	35.11	166	0.3242	25.1	1.8
ZH36-8.1a	107	0	0.004	0.0419	83.77	55	0.7086	19.1	2.6
ZH36-8.1b	40	0	0.004	0.0172	16.28	182	0.1754	29.6	2.5
ZH36-9.1	64	0	0.007	0.0429	89.66	17	0.7563	38.9	9.5

APPENDIX II. SHRIMP-PR U-Pb ANALYSES OF ZIRCON cont'd

ZH36-12.1	70	0	0.007	0.0422	55.28	100	0.4838	28.7	4.1
ZH36-18.1	74	0	0.005	0.0268	32.88	219	0.3063	19.7	2.7
ZH36-19.1	29	0	0.006	0.0511	87.62	21	0.7402	38.3	9.9
ZH36-24.1	48	0	0.006	0.0520	85.84	50	0.7249	18.4	4.5
ZH41-3.1	1066	6	0.006	0.0046	9.73	299	0.1233	19.4	0.6
ZH41-5.1	877	6	0.008	0.0248	49.13	152	152.0862	21.5	2.5
ZH41-8.1	1392	10	0.007	0.0057	6.43	263	0.0973	22.9	2.1
ZH41-10.1	994	8	0.008	0.0078	11.58	249	0.1380	22.9	2.6
ZH41-18.1	1035	5	0.005	0.0081	13.81	285	0.1556	19.4	1.2
ZH41-21.1	1377	6	0.005	0.0079	18.07	259	0.1893	20.4	1.2
Z4-6.4	4209	7	0.002	0.0003	1.31	309	0.0569	20.5	0.1
Z4-5.1	2252	4	0.002	0.0009	1.58	292	0.0590	21.7	0.2
Z4-12.1	1563	49	0.032	0.0006	1.70	202	0.0601	31.4	13.4
Z4-11.1	2823	8	0.003	0.0001	0.83	98	0.0539	64.6	23.8
Z32-5.1	1539	2185	1.466	0.0005	0.72	330	0.0521	19.4	0.4
Z32-10.1	777	19	0.026	0.0067	5.83	382	0.0924	15.9	0.3
Z32-11.1	62	2	0.030	0.0081	17.69	65	0.1880	81.7	51.7